BRNO UNIVERSITY OF TECHNOLOGY

Faculty of Mechanical Engineering

BACHELOR'S THESIS

Brno, 2024 Sára Hrdinová



BRNO UNIVERSITY OF TECHNOLOGY

VYSOKÉ UČENÍ TECHNICKÉ V BRNĚ

FACULTY OF MECHANICAL ENGINEERING

FAKULTA STROJNÍHO INŽENÝRSTVÍ

INSTITUTE OF PHYSICAL ENGINEERING

ÚSTAV FYZIKÁLNÍHO INŽENÝRSTVÍ

INFLUENCE OF THE EPITAXIAL STRAIN AT THE LATERAL THIN FILM-STRIPE INTERFACE ON THE FERROMAGNETIC-ANTIFERROMAGNETIC PHASE COEXISTENCE IN FERH

VLIV EPITAXNÍHO NAPĚTÍ NA KOEXISTENCI FEROMAGNETICKÉ A ANTIFEROMAGNETICKÉ FÁZE NA BOČNÍM ROZHRANÍ MEZI TENKOU VRSTVOU A PROUŽKEM FERH

BACHELOR'S THESIS

BAKALÁŘSKÁ PRÁCE

AUTHOR Sára Hrdinová

AUTOR PRÁCE

SUPERVISOR Ing. Oleksii Zadorozhnii

VEDOUCÍ PRÁCE

BRNO 2024



Assignment Bachelor's Thesis

Institut: Institute of Physical Engineering

Student: Sára Hrdinová

Degree programm: Physical Engineering and Nanotechnology

Branch: no specialisation

Supervisor: Ing. Oleksii Zadorozhnii

Academic year: 2023/24

As provided for by the Act No. 111/98 Coll. on higher education institutions and the BUT Study and Examination Regulations, the director of the Institute hereby assigns the following topic of Bachelor's Thesis:

Influence of the epitaxial strain at the lateral thin film-stripe interface on the Ferromagnetic-Antiferromagnetic phase coexistence in FeRh

Brief Description:

FeRh is an equiatomic magnetically ordered alloy which can undergo a temperature–induced magnetic phase transition from Antiferromagnetic (AF) to Ferromagnetic (FM) state close to 370K. Over the course of the phase transition from AF to FM state, phase coexistence is present. When transforming to a FM state, the main structural difference is the slight expansion of the lattice parameter. When chemically ordered FeRh is grown in the form of thin films epitaxially on MgO substrates, this leads to compressive strain which stabilizes the AF phase and increases the transition temperature when compared to bulk samples.

After patterning of the film, with decreasing lateral size of the structures the compressive strain is relaxed laterally, which decreases the phase transition temperature within the patterned structures. This difference between phase transition in patterned and full films could in principle allow us to create well defined areas of phase coexistence, where the patterned wire in contact with the full film would remain in the ferromagnetic phase, while full film would already have transitioned to the antiferromagnetic state.

We would like to investigate the phase coexistence regime at the lateral boundary between the thin film and stripe geometry of FeRh thin films. Depending on the width of the stripe, the length of the stripe, thin film thickness as well as the boundary conditions (closed or open–ended stripe) we expect to get different results for the FM–AF phase interface presence and phase coexistence conditions at the lateral boundary between the stripe and the film.

This study would show how exactly strain influences the phase coexistence in laterally varied geometries of FeRh (full film to stripe transition). Furthermore, establishing the geometry which provides the most well defined FM-AF phase boundary would enable us to study the possible magnetic interactions between the FM and AF phases in the future.

Bachelor's Thesis goals:

- 1. Literature search on the topic of magnetic properties and the influence of strain in epitaxial FeRh thin films.
- 2. Preparation of FeRh full thin films of different thicknesses and basic characterization using Vibrational Sample Magnetometry.
- 3. Characterization of the lithographically patterned FeRh thin film samples using Magnetic Force Microscopy at the lateral boundary between thin film and stripe geometries at varied temperatures, stripe widths, and thin film thicknesses.

Recommended bibliography:

- 1. KUMAR, H., CORNEJO, D. R., MORELHAO, S. L., KYCIA, S., MONTELLANO, I. M., ÁLVAREZ, N. R., ALEJANDRO, G. and BUTERA, A. Strain effects on the magnetic order of epitaxial FeRh thin films. Journal of Applied Physics. 2018. Vol. 124, no. 8. DOI 10.1063/1.5020160.
- 2. ARREGI, Jon Ander, CAHA, Ondřej and UHLÍŘ, Vojtěch. Evolution of strain across the magnetostructural phase transition in epitaxial FeRh films on different substrates. Physical Review B. 2020. Vol. 101, no. 17. DOI 10.1103/physrevb.101.174413.
- 3. SUZUKI, Ippei, KOIKE, Takayoshi, ITOH, Mitsuru, TANIYAMA, Tomoyasu and SATO, Tetsuya. Stability of ferromagnetic state of epitaxially grown ordered FeRh thin films. Journal of Applied Physics. 2009. Vol. 105, no. 7. DOI 10.1063/1.3054386.

Deadline for submission Bachelor's Thesis i 2023/24	s given by the	Schedule of the Academic year
In Brno,		
	L. S.	
prof. RNDr. Tomáš Šikola. CSc.	-	doc Ing .liří Hlinka Ph D

FME dean

Director of the Institute

Abstrakt

Ekviatomická slitina FeRh vykazuje fázový přechod z antiferomagnetického do feromagnetického uspořádání při teplotě kolem 350 K. Díky tomu se stává ideálním materiálem pro studium výměnných interakcí mezi ferromagnetickou a antiferomagnetickou fází v rámci systému tvořeného jedním materiálem. Díky relaxaci kompresivního epitaxního napětí způsobeného substrátem MgO na okrajích struktur a následné stabilizaci feromagnetické fáze, bychom mohli vytvořit vhodné rozhraní mezi relaxovaným feromagnetickým drátkem a napjatou antiferomagnetickou vrstvou.

V této práci jsou nejprve popisány magnetické vlastnosti materiálů, jejich původ a vlastnosti slitiny FeRh s důrazem na fázovou přeměnu. Dále práce obsahuje shrnutí aktuálních výzkumů a článků, týkajících se nukleace fázových domén na strukturovaných i souvislých vrstvách. K samotným měřením byly použity techniky jako je magnetronové naprašování, kterým byly nadeponovány vrstvy FeRh o tloušťkách 36 nm a 180 nm. Po úpravě vrstev pomocí elektronové litografie byly charakterizovány pomocí mikroskopie magnetických sil. Tato měření ukazují, že relaxave napětí výrazně závisí na orientaci proužku vzhledem ke krystalové struktuře substrátu. Pro orientaci 0° je vliv substrátu výraznější než pro 45°. Vrstva FeRh tloušťky 36 nm netvoří souvislé rozhraní na proužcích šířky 1000 nm. Místo toho vytváří malé domény, které vypovídají o rozložení napětí ve struktuře. Silnější vrstvy tloušťky 180 nm nám poskytují jasně definovaného rozhraní pro drátky delší něž 25 µm. Rozhraní bylo dosaženo pro šířky proužků od 1250 nm do 300 nm. U struktur s širšími proužky se feromagnetická fáze na okrajích souvislé vrstvy spojuje s feromagnetickou fází v drátku a tím zakřivuje rozhraní. Toto spojení se postupně přerušuje u tenších proužků s rozměry 800 nm a 600 nm. Proužek šířky 300 nm vykazuje jasné rozhraní mezi svými kraji, které je kompletně odděleno od souvislé vrstvy.

Summary

An equiatomic alloy FeRh exhibits a phase transition from antiferromagnetic to ferromagnetic ordering at a temperature about 350 K. This makes it an ideal material for studying exchange interactions between ferromagnetic and antiferromagnetic ordering within a single material system. In this work, we investigate the relaxation of the compressive epitaxial strain caused by nanopatterning of the FeRh film. Relaxation of this strain leads to the stabilization of the ferromagnetic phase, which could lead to the formation of a suitable interface between the relaxed ferromagnetic nanostripe and the compressed antiferromagnetic film.

In this bachelor thesis we first describe in detail the magnetic properties of the materials and properties of the FeRh alloy with the emphasis on the phase transformation. Our experiments supported by recent literature research include depositing FeRh layers with thicknesses of 36 nm and 180 nm. After patterning by electron beam lithography, the samples were characterised using Magnetic Force Microscopy. These measurements show that the strain relaxation is strongly dependent on the orientation of the nanostripe with respect to the crystal structure of the substrate. For an orientation of 0°, the strain relaxation is more pronounced than for 45°. The 36 nm thin FeRh layers do not form a continuous phase boundary between the nanostripe and the full film in 1000 nm wide nanostripes. Instead, they form small domains that are indicative of the strain distribution in the structure. Layers of 180 nm thickness show a phase coexistence between the nanopatterned stripe and the film for stripes longer than 25 µm. Well-defined interfaces have been achieved for stripe widths from 1250 nm to 300 nm. For structures with wider stripes, the ferromagnetic phase at the edges of the continu-

ous layer merges with the ferromagnetic phase in the nanostripe, thereby curving the interface. This merging is gradually broken at the interface in the thinner stripe with dimensions $800\,\mathrm{nm}$ and $600\,\mathrm{nm}$. The stripe of width $300\,\mathrm{nm}$ shows a clear interface between its sides.

Klíčová slova

Feromagnetismus, Antiferomagnetismus, FeRh, Fázová přeměna, Epitaxní napětí, MFM, Mikroskopie magnetických sil, Fázový přechod vyvolaný napětím

Keywords

Ferromagnetism, Antiferromagnetism, FeRh alloy, Phase transition, Epitaxial strain, Magnetic, Force Microscopy, MFM, Strain-induced phase transition

HRDINOVÁ, S. Vliv epitaxního napětí na koexistenci feromagnetické a antiferomagnetické fáze na bočním rozhraní mezi tenkou vrstvou a proužkem FeRh. Brno: Vysoké učení technické v Brně, Fakulta strojního inženýrství, 2024. 49 s. Vedoucí Ing. Oleksii Zadorozhnii.



I would like to sincerely thank Ing. Oleksii Zadorozhnii not only for the excellent guidance of my bachelor thesis, relevant comments and prompt answers, but also for the kind approach, patient explanation, constant support and entertaining conversations.

I would also like to thank the Nanomagnetism and Spintronics research group at CEITEC, specifically M.Sc. Jon Ander Arregi Uribeetxebarria, Ph.D. for help with the sample fabrication and Vojtech Uhlir, Ph.D. for helpful advice and comments.

Velké poděkování bych chtěla také věnovat mé milující rodině, rodičům, prarodičům a příteli za neustálé zvedání nálady a podporu během celého studia, bez které bych to nezvládla.

Czech Nano
Lab project LM2023051 funded by MEYS CR is gratefully acknowledged for the financial support of the measurements/sample fabrication at CEITEC Nano Research Infrastructure.

Sára Hrdinová

Contents

In	trod	uction	3						
1	Fun	adamentals of magnetism	5						
	1.1	Classical mechanics	5						
	1.2	Quantum magnetism	7						
	1.3	Exchange interactions	9						
	1.4	Types of magnetic order	12						
		1.4.1 Paramagnetism	12						
		1.4.2 Ferromagnetism	13						
		1.4.3 Antiferromagnetism	14						
	1.5	Magnetic anisotropy	14						
f 2	FeR	FeRh alloy							
	2.1	FeRh first order phase transition	18						
	2.2	Epitaxial strain and its effect on the transition	21						
	2.3	State of the art	22						
		2.3.1 Nucleation of phase domains	23						
		2.3.2 Phase domains in patterned films	25						
3	Exp	Experimental techniques 2							
	3.1	Magnetron sputtering	27						
	3.2	Vibrating Sample Magnetometry	28						
	3.3	Atomic Force Microscopy	28						
	3.4	Magnetic force microscopy (MFM)	30						
4	San	Sample Characterisation							
	4.1	Sample with 36 nm thick FeRh layer	34						
	4.2	Sample with 180 nm thick FeRh layer	37						
C	onclu	asions	43						
B	ibliog	graphy	45						

Introduction

The demand for low power and high speed memory has increased in recent years. Magnetic random access memory (MRAM) has the potential to enable low-power consumption memory storage. MRAM technology is based on magnetoresistance principle, which conventionally requires a synthetic antiferromagnet (SAF) reference layer, or alternatively a ferromagnetic layer exchange-coupled to an antiferromagnetic layer, which gives ferromagnetic layer unidirectional anisotropy and makes it point preferentially along a single direction even without any applied field. This effect is commonly referred to as exchange bias. What is more, there is an ongoing wave of research [1] into manipulation of this unidirectional anisotropy which on its' own could be used as a form of memory, or alternatively could be used to improve the performance of MRAMs, including storage capacity, power dissipation and advanced media [2], [3]. Exploiting exchange bias for memory storage is a hot topic in many papers and literature. However, the origin and behavior of this interaction remains largely unknown. The investigation of this phenomenon is possible by measuring magnetoresistance of the ferromagnetic thin film coupled to the antiferromagnetic layer. Most of ferromagnetic and antiferromagnetic bilayers in the literature are composed of vastly different materials, which makes the study of exchange bias challenging and very particular to chosen materials. Equiatomic alloy of Fe and Rh experiences a first order phase transition between antiferromagnetic and ferromagnetic order at 350K, making it potentially an ideal material for the study of exchange bias on the most simple level. In the range of about 10 K, the coexistence of the phases occurs, which we can use to study interactions between antiferromagnetic and ferromagnetic phase within the same material. With the increase of temperature, ferromagnetic domains nucleate and propagate throughout the antiferromagnetic layer. However, the location of these domains is random and does not provide us with a well defined interface required for studying the exchange bias.

The phase transition can be induced by magnetic field, defects or strain. We focus on the strain induced phase transition, in particular epitaxial strain, which is in FeRh films on MgO substrate compressive and shifts the phase transition to higher temperatures. If we form patterned structures, the epitaxial strain relaxes at the edges of the structure and allows the phase transition to occur at lower temperatures. The aim of our work is to study the influence of the epitaxial strain on the phase transition in patterned structures and find the most suitable phase interface that could later be used for magnetoresistive measurements. FeRh provides us with a single-material, two-phase system that could allow us to understand exchange bias better.

1. Fundamentals of magnetism

It is known, that materials have different magnetic properties. Some exhibit mutual magnetic forces even without an external magnetic field, while others appear to be non-magnetic and their magnetic behaviour might appear only with an external field. The main cause of this magnetic behaviour are in fact single atoms with non-zero total angular momentum \mathbf{J} , which is a sum of spin and orbital part.

Classical mechanics can be useful to explain some of the magnetic phenomena, but the classical approach is incomplete in many instances and we must be very careful in its application. If we think of the atom according to the Bohr model, i.e. we consider the electrons as localized spheres orbiting around a positively charged nucleus on an individual energy levels, we can briefly derive the magnitude of orbital angular momentum **L** for electron. However, there is no classical derivation for spin angular momentum **S** demonstrated in experiments like a Stern - Gerlach experiment. In the following sections I will be presenting the essential formulas for understanding the magnetic behaviour of various materials using particularly simpler classical principles and proceed to a more complex quantum approach when necessary [4].

1.1 Classical mechanics

Magnetic susceptibility

The total response to the external field of a material is characterized by magnetic susceptibility χ :

$$\chi = \frac{\mathbf{M}}{\mathbf{H}}.\tag{1.1}$$

Magnetization M characterizes the sum of magnetic moments μ per volume V, and H describes the magnetic field. The magnetic induction B can be then calculated as:

$$\mathbf{B} = \mu_0 \mathbf{H} + \mu_0 \mathbf{M} = \mu_0 (1 + \chi) \mathbf{H} = \mu_0 \mu_r \mathbf{H}, \tag{1.2}$$

where μ_0 is permeability of vacuum and μ_r is relative permeability.

Gyromagnetic ratio

The magnetic moment of an atom responsible for the magnetic behaviour is composed of magnetic moments of its particles such as protons, neutrons and electrons. Magnetic

moments of electrons contribute the most to the total magnetic moment, that is why we will be focusing mainly on them and their orientation.

According to the Bohr model (shown in the Figure 1.1), we expect, that the electron with both mass and negative charge orbiting a circle around nucleus creates not only current loop with a magnetic moment μ , but also has its own angular momentum \mathbf{L} . If I is current caused by orbiting electron and S is area enclosed by its trajectory. The magnetic moment can be calculated by integrating over area S the relation [5]:

$$d\mu = IdS, \tag{1.3}$$

Proportionality between the magnetic moment μ and the angular momentum \mathbf{L} is called gyromagnetic ratio γ and is verified by Einstein de Haag's experiment.

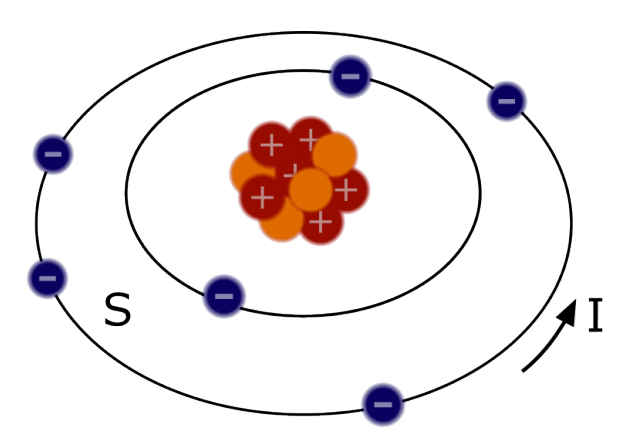


Figure 1.1: Bohr's model of an atom.

To find the value of γ , we consider the orbit radius R, magnitude of velocity v and rotationally symmetric distribution of mass m and charge q. We need to substitute $qv/2\pi R$ for current I and surface of the loop created by electron's trajectory for S in equation (1.3). Subsequently, by applying equation for classical angular momentum $\mathbf{L} = \mathbf{R} \times m\mathbf{v}$, we obtain:

$$\mu = \frac{q}{2m} \mathbf{L} = \gamma \mathbf{L}. \tag{1.4}$$

For particles, the value of γ differs. It is convenient for us to establish dimensionless constant called g-factor g as:

$$\gamma = g \frac{q}{2m}.\tag{1.5}$$

The derived magnetic moment of the electron in the equation 1.4 is called orbital magnetic moment $\mu_{\mathbf{o}}$ and \mathbf{L} is called orbital angular momentum. From substituting the charge q with -e we get the relation:

$$\mu_{\mathbf{o}} = -\frac{e}{2m}\mathbf{L}.\tag{1.6}$$

Equation 1.6 displays orbital angular momentum, but the electron has also quantity known as spin S, the intrinsic angular momentum, which we can naively imagine as the rotation around the electron axis. It is unfortunately not possible to concisely derive the expression for spin angular momentum μ_s , but from the article [6] we know, that

its g-factor $g = 2.002319... \approx 2$ [4] and therefore [7]:

$$\mu_{\mathbf{s}} = -\frac{e}{m}\mathbf{S}.\tag{1.7}$$

1.2 Quantum magnetism

Spin angular momentum is not the only case where the classical approach fails in explaining magnetic properties. Explaining ferromagnetism, antiferromagnetism and other orderings is not possible without considering the wave nature of particles, Pauli's exclusion principle and quantum mechanics in general.

Orbital and spin angular momentum

Our next task is to determine the value of angular momentum. Just as momentum is related to translation, angular momentum is related to rotation. It will therefore be convenient for us to use a spherical coordinate system. Particle-like electron is described by a wave function $\psi(\Theta, \Phi, r, t)$ that belongs to Hilbert space and is a solution of the Schrödinger equation. We want to have two commutative operators, because then it is possible to find a complete set of simultaneous eigenvectors with indices m_o and l. All components of the angular momentum commutate with Casimir operator $\hat{\mathbf{L}}^2$. Eigenfunctions take the form of:

$$\hat{\mathbf{L}}_z Y_{l,m_o}(\theta, \Phi) = \hbar m_o Y_{l,m_o}(\theta, \Phi)$$

$$\hat{\mathbf{L}}^2 Y_{l,m_o}(\theta, \Phi) = \hbar^2 l(l+1) Y_{l,m_o}(\theta, \Phi),$$
(1.8)

where Y_{l,m_o} is the eigenfunctions for orbital angular momentum. To justify the form of the function, we use the following considerations: because indicies m_o and l are are unitless, the reduced Planck constant must be present to preserve the units. Also because the operators are Hermitian, both eigenvalues must be real. In order to obtain additional conditions for the indicies, we have to substitute the operators and solve the differential equations. From the periodic conditions of the first equation we find that m_o is an integer.

The second equation is slightly more complex. The operator $\hat{\mathbf{L}}^2$ is equal to the azimuthal part of the Laplace operator in spherical coordinates multiplied by $-\hbar^2$, so it is not surprising that the solutions are spherical harmonic functions. When solving this partial differential equation in detail, we get two new crucial conditions (1.9), that ensure the solution is neither trivial nor divergent.

$$l = 0, 1, 2, 3, ...$$

 $m_o = -l, -l + 1, ..., 0, ..., l - 1, l$ (1.9)

Index l is called azimuthal and m_o magnetic quantum number [8].

We now proceed to find relations for the spin angular momentum. The eigenfunctions for spin angular momentum are analogous to the eigenfunctions of orbital angular

momentum 1.8:

$$\hat{\mathbf{S}_z}\mathbf{I} = \hbar m_s \mathbf{I}$$

$$\hat{\mathbf{S}^2}\mathbf{I} = \hbar^2 s(s+1)\mathbf{I}.$$
(1.10)

However the spin angular momentum operators $\hat{\mathbf{S}}_x$, $\hat{\mathbf{S}}_y$ and $\hat{\mathbf{S}}_z$ are represented by 2×2 matrices:

$$\hat{\mathbf{S}}_x = \frac{\hbar}{2} \begin{pmatrix} 0 & 1\\ 1 & 0 \end{pmatrix}, \quad \hat{\mathbf{S}}_y = \frac{\hbar}{2} \begin{pmatrix} 0 & -i\\ i & 0 \end{pmatrix}, \quad \hat{\mathbf{S}}_z = \frac{\hbar}{2} \begin{pmatrix} 1 & 0\\ 0 & -1 \end{pmatrix}. \tag{1.11}$$

These spin angular momentum operators consist of so-called Pauli spin matrices, denoted by the Greek letter σ_x , σ_y and σ_z respectively, multiplied by the constant $\hbar/2$.

Again, certain conditions hold for their eigenvalues. Number s called spin quantum number has specific value for different particles. It is an integer for all bosons and a half-odd-integer for all fermions. Number m_s is spin magnetic quantum number with values:

$$m_s = -s, -s + 1, ..., 0, ..., s - 1, s.$$
 (1.12)

Electron has s = 1/2 and $m_s = \pm 1/2$ [9]. Thanks to these eigenfunctions for spin and orbital angular momentum, we obtain the following outcomes. Only the size of $\hat{\mathbf{L}}$ (resp. $\hat{\mathbf{S}}$) and its projection onto the z-axis $\hat{\mathbf{L}}_{\mathbf{z}}$ (resp. $\hat{\mathbf{S}}_{\mathbf{z}}$) can be measured simultaneously with values:

$$L_z = m_o \hbar \qquad S_z = m_s \hbar$$

$$L = \sqrt{l(l+1)}\hbar \quad S = \sqrt{s(s+1)}\hbar.$$
(1.13)

Combining these relations with (1.6) and (1.7) gives us an expression for the measurable z-axis projection of the electron magnetic moment in which an important constant, the Bohr magneton μ_B , appears [7]:

$$\mu_{o,z} = -\frac{e}{2m_e} L_z = -\frac{e\hbar}{2m_e} m_o = -\mu_B m_o$$

$$\mu_{s,z} = -\frac{e}{m_e} S_z = -2\frac{e\hbar}{2m_e} m_s = -2\mu_B m_s.$$
(1.14)

When considering the quantization of the angular momentum of both the spin and orbital components, it is important to contextualise them with other quantum numbers and point out the significant consequences. Principal quantum number n gives us another condition for azimuthal quantum number l, because the size of l must not exceed n-1. We also define total angular momentum \mathbf{J} , which is a vector sum of \mathbf{L} and \mathbf{S} [7]:

$$\mathbf{J} = \mathbf{L} + \mathbf{S}.\tag{1.15}$$

The total magnetic moment μ_{tot} , which is finally equivalent to the total magnetic dipole of the particle is given by expresion:

$$\mu_{\text{tot}} = g_j \frac{-e}{2m} \mathbf{J},\tag{1.16}$$

where g_j is a Landé factor.

Atom in magnetic field

The energy operator of an atom, Hamiltonian $\hat{\mathbf{H_0}}$, is a sum of Hamiltonian $\hat{\mathbf{H_i}}$ of each *i*-th electron. Without external magnetic field \mathbf{B} takes form:

$$\hat{\mathbf{H}}_0 = \sum_{i=1}^{Z} \left(\frac{\mathbf{p_i^2}}{2m} + V_i \right). \tag{1.17}$$

The $\mathbf{p_i}$ is momentum of the *i*-th electron, the V_i is potential energy of the *i*-th electron and m stands for electron mass. Hamiltonian $\hat{\mathbf{H}}$ of an atom with \mathbf{B} present is composed of $\hat{\mathbf{H_0}}$ and two other terms:

$$\hat{\mathbf{H}} = \sum_{i=1}^{Z} \left(\frac{\mathbf{p_i^2}}{2m} + V_i \right) + \mu_B(\mathbf{L} + g\mathbf{S})\mathbf{B} + \frac{e^2}{8m} \sum_{i=1}^{Z} (\mathbf{B} \times \mathbf{r_i})^2.$$
 (1.18)

In this equation 1.18 the r_i is position of the *i*-th electron, e is elementary charge and the second term $\mu_B(\mathbf{L}+g\mathbf{S})$ is equal to total magnetic moment $g_j\mu_B\mathbf{J}$ and is responsible for paramagnetism, which corresponds to $\chi>0$. Because the total angular momentum is zero for all fully occupied shells, the paramagnetism is present only in atoms with valence electrons and increases with its number. On the contrary diamagnetism ($\chi<0$) caused by the third component does not depend on any angular momentum and is present in every material [5]. In some literature (for example [10]) another more intuitive idea about the origin of diamagnetism is given. This idea based on principle of electromagnetic induction consists of the formation of current loops, which induce magnetic field as counteract to the change of magnetic flux.

1.3 Exchange interactions

We already know that the phenomena of paramagnetism and diamagnetism are responsible for the effects on the external magnetic field, but this still does not explain spontaneous magnetization of some materials without applied field, because without considering the individual interactions acting on the magnetic moment, the most probable state of a matter is zero magnetization **M** due to the random orientation of magnetic moments.

The first magnetic interaction that probably comes to mind that could explain this self-ordering is the dipole-dipole for most people is the dipole-dipole. However, the calculations show that this interaction is weak and has a noticeable effect only at low

temperatures. The magnetic arrangement is caused by a much stronger interaction, called exchange interaction. This interaction is nothing more than the consequence of the Coulomb electrostatic interactions among electrons and Pauli exclusion principle. The cause of this interaction is spin-spin coupling (S-S coupling) [11].

Exchange interaction can be classified as direct, which takes place between electrons of neighbouring atoms or indirect, that occurs between electrons of more distant atoms and needs an intermediary. The direct interaction is less complex, but unfortunately is also not strong enough to explain the magnetic order, so the interactions we will focus on will be indirect exchange interactions.

For simplicity, let's consider two electrons with s = 1/2. As fermions, they are subject to the principle of indistinguishability of particles and must have an antisymmetric overall joint wave function. The spin part of the wave function can be in singlet state (S = 0) with energy E_S and anti-parallel spin orientation or triplet state (S = 1) with energy E_T and parallel spin orientation. Spin dependent term of Hamiltonian can be then written as:

$$\hat{\mathbf{H}}_{spin} = (E_T - E_S)\mathbf{S_1} \cdot \mathbf{S_2} = -2J\mathbf{S_1} \cdot \mathbf{S_2}. \tag{1.19}$$

Constant J is called exchange constant and S_1 , S_2 are spin operators for the two electrons. To obtain the Hamiltonian involving the mutual interactions of all electrons, we sum over all electrons and divide by two, because the interactions between ith and jth electron need to be included just once. The result is Hamiltonian of a Heisenberg model $\hat{\mathbf{H}}_H$.

$$\hat{\mathbf{H}}_H = -\sum_{i,j} J\mathbf{S_i} \cdot \mathbf{S_j} \tag{1.20}$$

Ferromagnetic ordering occurs when J > 0 and the spins are aligned parallel. Antiferromagnetic order has J < 0 and anti-parallel alignment [5].

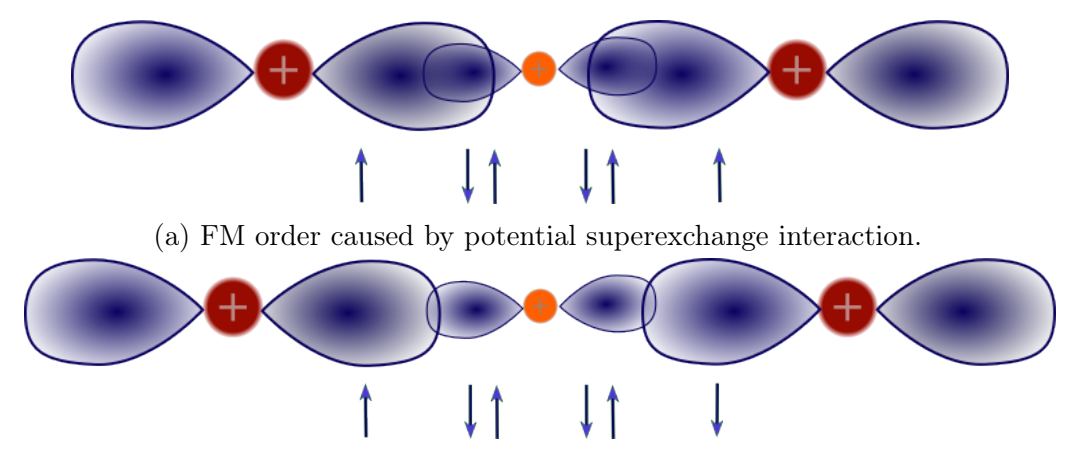
In some literature [11] there is the ferromagnetic interaction called potential and the antiferromagnetic called kinetic. This terminology stems from the idea that in potential exchange, the overlap of functions (and thus potential energy) is minimized by the addition of nodes, causing antisymmetry of the wave function and hence the symmetry of the spin part. Whereas in the kinetic, electron delocalization is allowed (and thus kinetic energy is minimized), leading to symmetric wave functions and antisymmetric spins. This description is as an example displayed in picture 1.2.

Although there are several types of exchange interactions, we will now mainly focus on the three types, that are attractive for us - superexchange, indirect exchange in metals and anisotropic exchange interactions.

Superexchange interaction

Superexchange interaction can be found in many insulators, which have magnetic ions interleaved with nonmagnetic anions (for example oxygen, nitrogen, fluorine). The overlap between magnetic ions is very small or none, therefore the interactions are indirect and mediated via intermediate oxygen atom. Superexchange interaction in

most cases leads to antifferomagnetic order, because during the kinetic exchange due to Pauli exclusion principle the electron lowers its kinetic energy by delocalizating [11], [5].



(b) AFM order caused by kinetic superexchange interaction.

Figure 1.2: Coupling in Mn-O. Adapted and edited from [12]

Indirect exchange interaction in metals

Unlike the electrons responsible for magnetism in insulators, the electrons responsible for magnetic behaviour in metals are delocalized. Exchange interaction in metals is called RKKY or itinerant exchange. It is mediated by conduction electrons, which are spin-polarized by localized magnetic moment. Spin polarized electrons then couple with magnetic moment in distance r. Based on the fact, that the exchange constant J_{RKKY} is proportional to $\cos(2k_F r)/r^3$, where k_F is radius of spherical Fermi surface, we can tell, that this interaction is long ranged and depending on r the order is either ferromagnetic or antiferromagnetic.

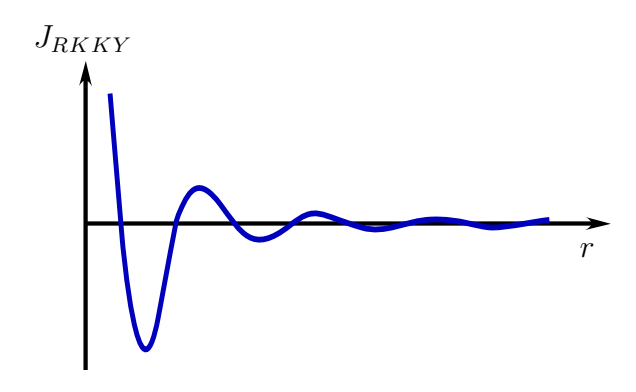


Figure 1.3: Damped oscillating waveform of the exchange constant.

Anisotropic exchange interaction

As we will see in the next section, spin-orbit coupling is the main cause of anisotropy. Exchange anisotropy is no different. The spin-orbit interaction acts as a mediator of indirect exchange, similar to oxygen in superexchange interaction.

The Hamiltonian $\hat{\mathbf{H}}_{DM}$ of this anisotropic exchange interaction between two spins $\mathbf{S_1}$ and $\mathbf{S_2}$, sometimes also called Dzyaloshinsky-Moriya interaction, is equal to:

$$\hat{\mathbf{H}}_{DM} = \mathbf{D} \cdot \mathbf{S_1} \times \mathbf{S_2}. \tag{1.21}$$

If the crystal field has inversion symmetry with respect to the centre between the two magnetic ions, the vector **D** disappears. The interaction attempts to align spins to be at right angles in a plane perpendicular to the **D**, so that the orientation ensured the negative energy. As a result, it often causes the spins to slightly rotate [5]. In practice, this interaction is present in thin films in contact with metals which have large orbital moment (Pt, Ru, Ta). Although this exchange interaction does not create a magnetic order directly, it creates strong anisotropy in the ferromagnetic film perpendicular to the heavy metal interface.

1.4 Types of magnetic order

Magnetic moments can have different periodic mutual orientations depending on the exchange interaction. The main types are paramagnetic, ferromagnetic, antiferromagnetic and ferrimagnetic order.

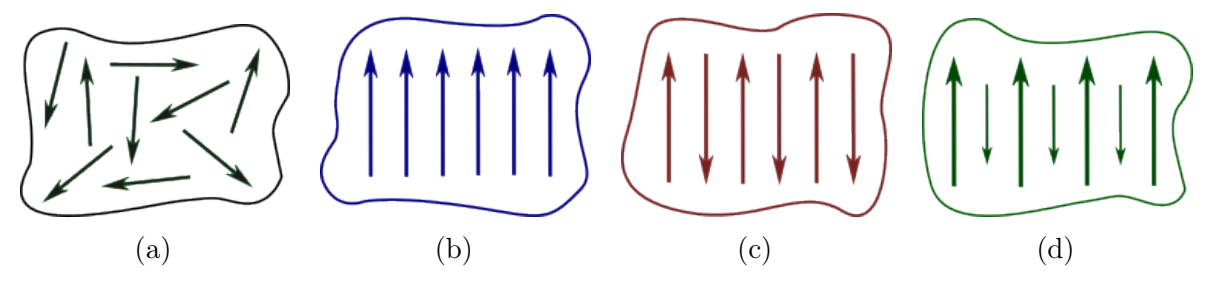


Figure 1.4: Ordering of magnetic moments in a) paramagnetic, b) ferromagnetic, c) antiferromagnetic and d) ferrimagnetic material.

Paramagnetic order consists of random orientation of magnetic moments, which mutually cancel out and no magnetization is measured. Ferromagnetic order has the moments oriented in one direction, which can be observed as spontaneous magnetization. In antiferromagnetic order the moments are arranged antiparallel and as with paramagnetics the material appears to be non-magnetic. Lastly, the ferrimagnetic order has antiparallel ordering of moments with different values, thus spontaneous magnetization can be measured [10].

1.4.1 Paramagnetism

In paramagnetism, thermal energy beats exchange energy and moments are randomly oriented. When subjected to an applied magnetic field, another energy called Zeeman joins the energy competition and tends to align the magnetic moments. For a system

of classical non-interacting moments, the magnetisation M is given by:

$$M = NM_0L(x). (1.22)$$

The value of the magnetization at 0 K is represented by M_0 , while the Langevin function is denoted by L(x). The N is number of moments per unit volume. The parameter x used in the Langevin function is the ratio between Zeeman energy and thermal energy. For small x higher terms of expanded Langevin function can be neglected and the high-temperature development can be written as:

$$M = C\frac{H}{T}. (1.23)$$

A gentle modification of the relation then gives Curie's law showed in Figure 1.5:

$$\chi = \frac{C}{T}. ag{1.24}$$

where C is Curie constant.

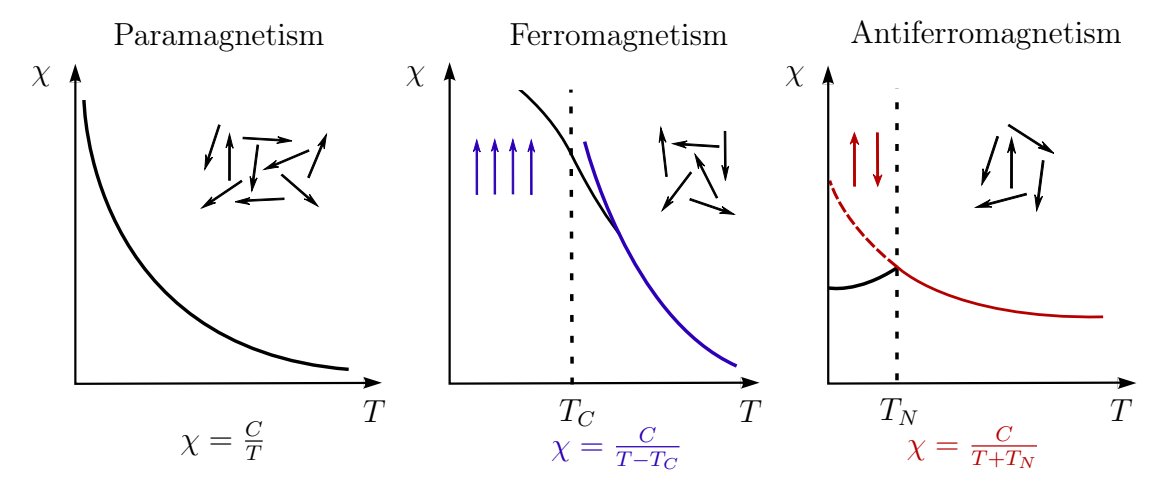


Figure 1.5: The evolution of magnetic susceptibility for different magnetic orderings. For paramagnetics, the magnetic susceptibility decreases with temperature as $\propto 1/T$. However, this dependence is present in all materials, since every substance becomes paramagnetic from a certain temperature. This temperature is called the Curie temperature T_C for ferromagnetics and the Néel temperature T_N for antiferromagnetics. Before reaching these temperatures, the development of susceptibility is complicated. Qualitatively, however, we know that the susceptibility of ferromagnetics is high at low temperatures because the magnetic moments are easily oriented in the external field direction. Temperature, however, increases the fluctuations of the moments and thus reduces susceptibility. On the contrary, for antiferromagnetics at low temperatures, magnetic moments cannot easily amplify the field and temperature fluctuations make this easier.

1.4.2 Ferromagnetism

The material exhibits ferromagnetic order only at relatively low temperatures. There always exists a Curie temperature T_C at which the thermal energy overcomes exchange

energy and the order becomes paramagnetic. At 0 K, the ferromagnetic material remains self-ordered, and external field only changes the orientation of the magnetisation \mathbf{M} of its' domains, so the value of χ is high. With increasing temperature the susceptibility keeps decreasing due to the effect of T forcing the magnetic moments to disorder. At the point $T = T_C$, the phase transition takes place and the susceptibility dependence becomes linear, as is typical for paramagnets. Ferromagnetic materials' susceptibility above the curie temperature follows the Curie-Weiss law [13]:

$$\chi = \frac{C}{T - T_C}. (1.25)$$

The C is again the Curie constant. This dependency is again plotted in the Figure 1.5. Bellow T_C the temperature dependence of χ is more complex.

1.4.3 Antiferromagnetism

The temperature of the phase transition from an antiferromagnetic to a paramagnetic order is named Néels temperature T_N (analogous to the Curie temperature). We can again describe the behaviour of the magnetic susceptibility χ at temperatures above T_N as:

$$\chi = \frac{C}{T + T_N},\tag{1.26}$$

which is again the Curie-Weiss law, but for $T_C = -T_N$ [5].

1.5 Magnetic anisotropy

We currently know that paramagnetism and diamagnetism are caused by interactions with the external field and ferromagnetism and antiferromagnetism by exchange interactions. Another observed feature is the varying behavior of magnetization for different directions of applied field: the magnetic anisotropy. The main causes of anisotropic behaviour are the spin-orbit coupling and dipolar interaction. Orientation along which the magnetization preferentially orients without any applied field is called the easy axis. On the other hand, orientation in which sample saturation requires high applied field is called the hard axis. Easy magnetization direction does not have to be defined only as one axis, but can be defined as multiple axes or even an entire plane [14], [10].

Magnetic anisotropy has several contributions, like exchange, which was reviewed in the previous section, shape and crystal (sometimes called magnetocrystalline) anisotropy, which includes also strain anisotropy.

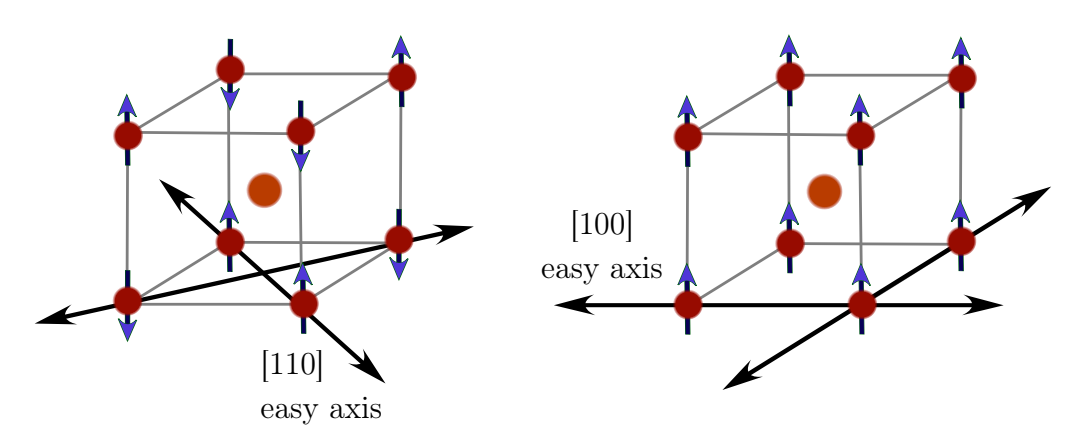


Figure 1.6: Biaxial (fourfold) magnetic anisotropy in two Iron Rhodium lattices. Based on data from article [15].

Crystal anisotropy

Crystal anisotropy comes from spin-orbit coupling (L-S coupling). The orbital moments are strongly attached to the lattice. When, for example, a magnetic field is applied, both spin and orbital magnetic moments want to face the same direction. Because of the strong bond between lattice and orbital moment, only spin moment can be reoriented, whereby it must overcome the L-S interaction. In unixial system the magnetocrystalline energy E_{ca} is often approximated as:

$$E_{ca} = K_{ca} \sin^2 \theta. \tag{1.27}$$

The angle θ is between easy axis and magnetization, K_{ca} is anisotropy constant [10].

Strain anisotropy

Strain in a ferromagnet can alter the magnetocrystalline anisotropy and thus influence the magnetic anisotropy. In equation for strain anisotropy energy E_{sa} :

$$E_{sa} = \frac{3}{2}\lambda\sigma\cos^2\theta,\tag{1.28}$$

the stress σ is expressed in the anisotropy constant as $K_{sa} = -\frac{3}{2}\lambda\sigma$, where the angle θ measures the direction of the magnetization relative to the direction of uniform stress and magnetostriction λ can be either positive or negative depending on the orientation. Magnetostricticion is the phenomenon, that describes magnetization changing the dimentions of material. It is an inverse effect to strain isotropy [10], [16].

Shape anisotropy

The dipolar interaction is generally responsible for the shape anisotropy contribution due to its long-range character. This contribution depends on the sample's shape and is particularly important in thin films, where it is largely responsible for the observed inplane magnetization. In the continuum approximation, the anisotropic demagnetizing field can describe the shape effect of the dipolar interaction in ellipsoidal ferromagnetic samples. The energy contribution E_{ha} per volume will be:

$$E_{ha} = \frac{1}{2}\mu_0 M_s^2 \cos^2 \theta. \tag{1.29}$$

Saturation magnetization is written as M_s and the angle with the film normal as θ [16].

2. FeRh alloy

After summarising the theoretical overview of magnetism and its origin, we will now move directly to the equiatomic FeRh alloy. We will describe its basic properties, focusing on the phase transition and related phenomena.

As the characteristics of alloys are significantly affected by both temperature and elemental composition, we will begin by examining a phase diagram for bulk FeRh in picture 2.1. Regarding the magnetic properties, the alloy can be ferromagnetic (FM), antiferromagnetic (AM) or even paramagnetic (PM) at low temperatures depending on the Rh concentration. When the temperature is raised above the Curie point T_C , the ordering is disrupted and the material becomes completely paramagnetic.

Each phase can have different atomic arrangements and lattice parameters, which may modify mechanical, magnetic and electrical properties. Therefore, we will now briefly describe the individual phases.

- Phase γ : phase with the PM face-centred cubic (FCC) structure, which has a complete solid solubility in the range between 1300 °C and 1394 °C. Phase can occur at each temperature below liquidus. Lattice constant is more than 3.7 Å.
- Phase δ : high-temperature phase that has PM body-centred cubic (BCC) structure and solubility up to a concentration of 3 % of Rh [17], [18].
- Phase α : low-temperature phase present when the Rh concentrations are up to about 20%, which has FM disordered BCC structure.
- Phase α' : low-temperature phase that occurs in the range from 20% to 50% Rh concentrations. It is a chemically ordered FM (alternatively PM at $T > T_C$) phase with CsCl lattice type.
- Phase α'' : low-temperature phase that occurs between 48 % and 55 % of Rh. This phase also has a chemically ordered CsCl structure but exhibits antiferromagnetic order.

We are interested in the phase transition of AF α'' to FM α' . This transition occurs in alloy Fe_{1-x}Rh_x with x in the range of 0.48 and 0.54 [19], [18]. At these concentrations, the transition occurs up to a temperature T_p of about 130 °C. The next transition appears above the Curie temperature, which ranges from approximately 380 °C to 500 °C [18]. These temperatures, especially the T_p , often considerably vary even for similar compositions, because the transition temperatures depend on sample preparation like heat treatment or external factors, which include external field or pressure. For example, for alloy with an equiatomic composition Fe₅₀Rh₅₀, values $T_p =$

65 °C and $T_C = 405$ °C were measured by [20]. According to another measurement [21], the values are $T_p = 92$ °C and $T_C = 407$ °C. The transition temperatures and lattice parameters for different Rh concentrations were compared in the paper [18].

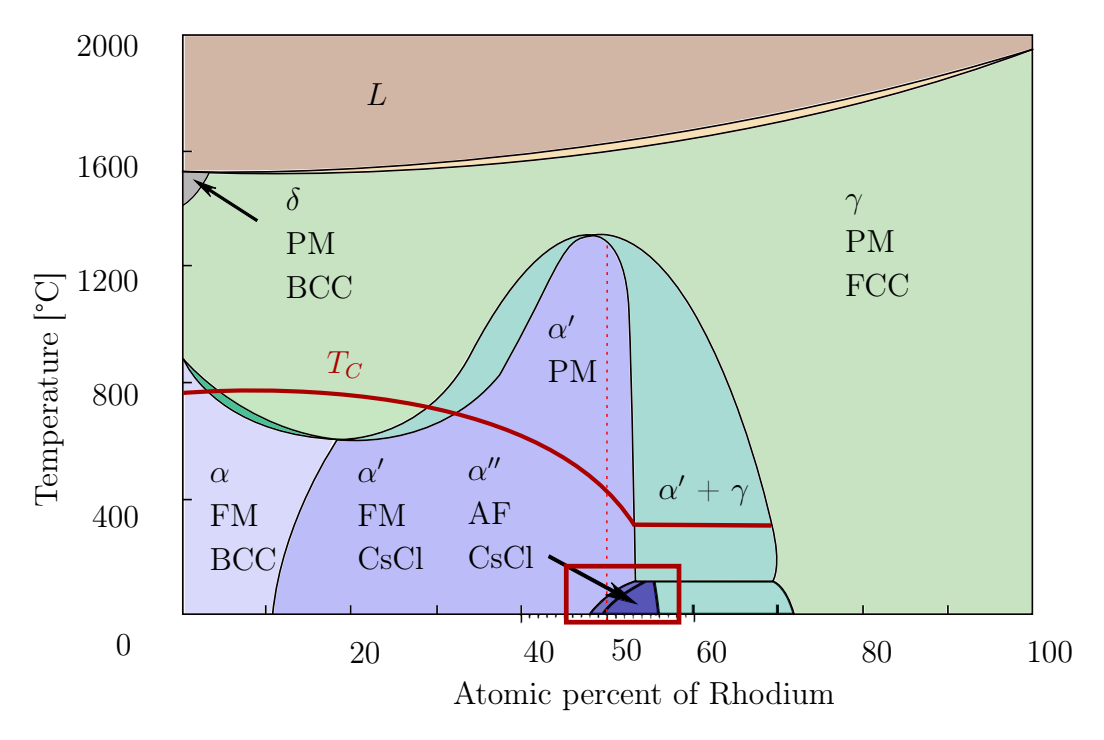


Figure 2.1: Phase diagram of FeRh. Red square highlights our region of interest, where the phase transition from AF to FM order takes place [18].

2.1 FeRh first order phase transition

The Gibbs free energy G is a suitable thermodynamic potential to describe phase transitions. Its form is obtained by modifying the first law of thermodynamics at a constant number of particles [22].

$$dU = TdS - pdV$$

$$dG = U - TS + pV = -SdT + VdP$$
(2.1)

Based on this potential G Paul Ehrenfest created phase transition classification to first and second order. The first order transition exhibits discontinuity in its first derivative of thermodynamic potentials, while the second type displays discontinuity in its second derivatives. Besides this difference, the first transition involves latent heat. If S is entropy, V volume, C_p specific heat at constant pressure and the κ_T compressibility at constant temperature, the first and second derivatives of Gibbs free energy are:

$$S = -\left(\frac{\partial G}{\partial T}\right)_{p}, \qquad V = \left(\frac{\partial G}{\partial p}\right)_{T},$$

$$C_{p} = -\left(\frac{\partial^{2} G}{\partial T^{2}}\right)_{p}, \qquad \kappa_{T} = -\left(\frac{\partial^{2} G}{\partial p^{2}}\right)_{T}.$$

$$(2.2)$$

This classification is limited to a thermodynamic view of the phenomena. According to L. D. Landau, our phase transition in FeRh has discontinuous order parameter (magnetization), so it belongs to first order transition in Ehrenfest's sense and contains latent heat [23].

The presence of latent heat in FeRh is associated with huge change in total entropy. This change is much larger than the change of lattice entropy, therefore papers such as [24] state that the band-electron entropy plays an important role in this first order phase transition and is even its main driving force. Controlling the transition could lead to a magneto-caloric effect, where the temperature can be changed by isothermal or adiabatic application of weather magnetic field or strain field. When the magnetic field is applied, then we speak of a giant magnetocaloric effect (MCE). When the strain field or pressure is applied, we speak of a giant barocaloric effect [17].

Although both phases α'' and α' have the same chemically ordered CsCl structure, the crystal lattice changes during the phase transformation by increasing the lattice parameter from 2.987 Å to 3.005 Å [25]. The values of the lattice parameter from different sources deviate mostly by orders of thousandths of Å. Changing this parameter will result in the short-range Fe-Fe and Fe-Rh interactions favoring FM order overcoming the long-range Fe-Fe interactions between iron atoms preferring AF order, which causes a flip of the atoms' spins [19].

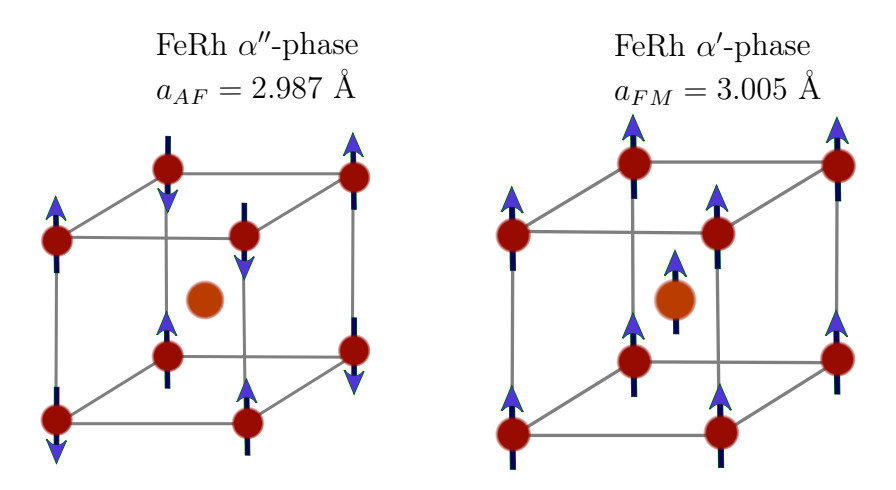


Figure 2.2: Change of the lattice parameter and magnetic order during phase transition. Adapted from [25].

The two phases have different atomic magnetic moments for both Fe and Rh. The magnetic moment of the α' – phase or the of α'' – phase Fe is greater than $\approx 3~\mu_{\rm B}$ [26]. In particular, the article [27] states that in FM phase the moments $\mu_{\rm FeII} = 3.2~\mu_{\rm B}$ and $\mu_{\rm RhII} = 0.9~\mu_{\rm B}$. For the AF phase, according to [28], $\mu_{\rm FeI} = 3.3~\mu_{\rm B}$ and $\mu_{\rm RhI}$ is zero. Compared to a pure iron in α -phase with lattice parameter 2.84 Å with magnetic moment of 2.2 $\mu_{\rm B}$ [29], is the magnetic moment of α' and α'' about 1/3 larger.

During this transition, other parameters change in addition to volume or entropy. These include magnetisation and resistance (shown in figure 2.3).

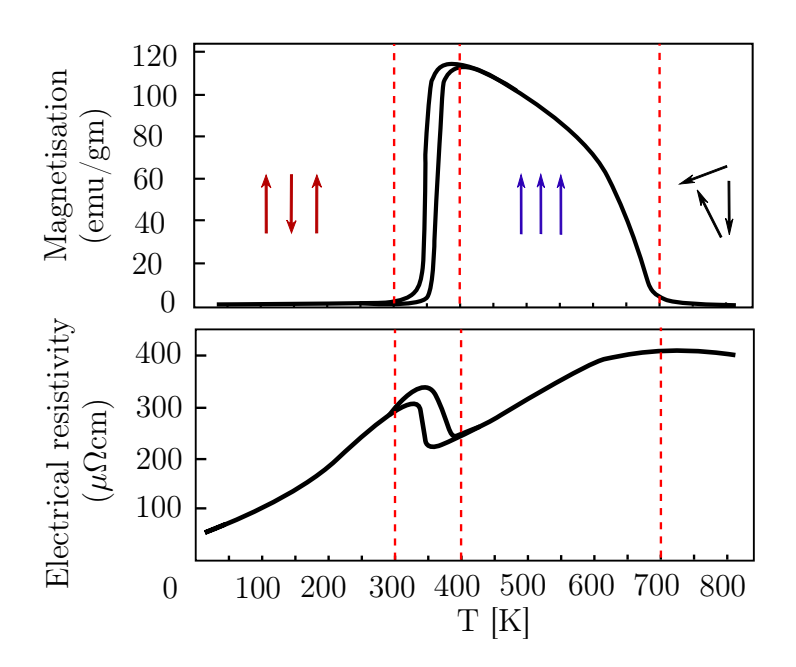


Figure 2.3: Change in properties of $Fe_{48}Rh_{52}$ adapted from [30]. In the first magnetisation plot with 5 kOe external magnetic field, the material initially appears to be non-magnetic, around the temperature of 350 K a transformation occurs, which is manifested by a sharp increase in magnetization. After reaching a maximum, when the whole sample is FM, the magnetisation decreases to zero and at $T_C = 675$ K the sample is paramagnetic. In the second plot the resistivity versus temperature is shown; its increase with temperature is influenced by a phase transformation whose temperature corresponds to the first plot.

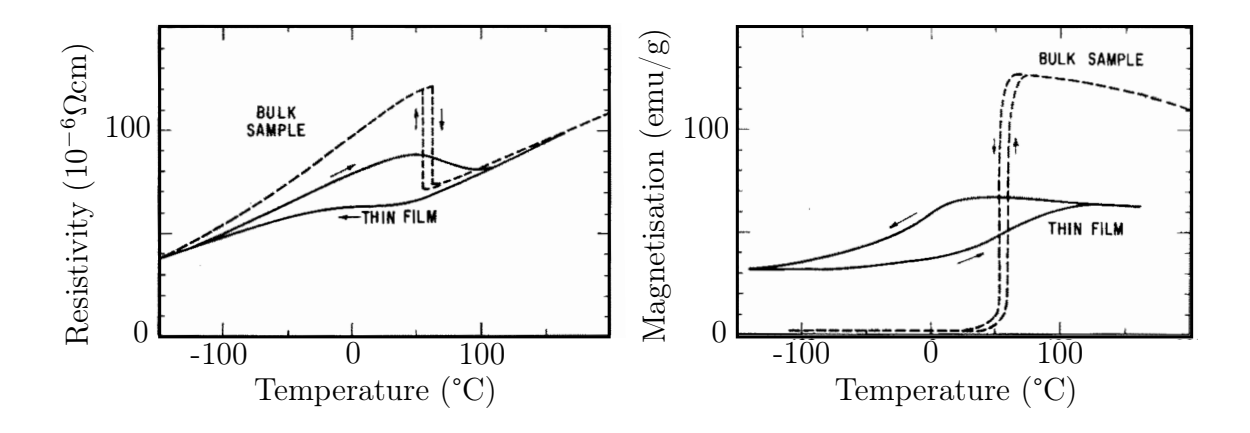


Figure 2.4: Comparison of magnetisation and resistivity change with temperature during the phase transition for bulk and thin film. Taken from [31].

So far we have been primarily talking about bulk FeRh. For thin films we can observe similar phenomena, but there are a couple of changes. The difference between bulk and thin film was observed in [31], which states that the lattice parameter remains consistent, but from the resistivity and magnetisation measurements in picture 2.4 is

clear, that the transition temperature is shifted and transition broadening with large thermal hysteresis are observed.

Controlling the phase-transition temperature is widely discussed topic. The temperature is significantly influenced by many factors such as external magnetic field [19], [32], defects and ion beam irradiation [33], topography [34], sample treatment [35] like annealing, alloying of the Fe–Rh composition with small amounts of other elements [36], and last but not least - mechanical strain, which is the subject of the following section. For example alloying FeRh with other elements can change the temperature by hundreds of Kelvin [37]. Magnetic field can shift the temperature of Pd-doped Fe-Rh by 100 K [38]. The magnetisation curve depending on temperature can be also strongly distorted by different sample treatment [39].

2.2 Epitaxial strain and its effect on the transition

Many articles point out the influence of the substrate on the phase transformation temperature T_p . For example, the article [40] observes the transition of FeRh on Al_2O_3 and MgO substrates. From the figure 2.5, it is clear that the temperature T_p shifts by about 20 °C. The article [41] compares a sample attached to a substrate and then after peeling the substrate, which again affects the T_p .

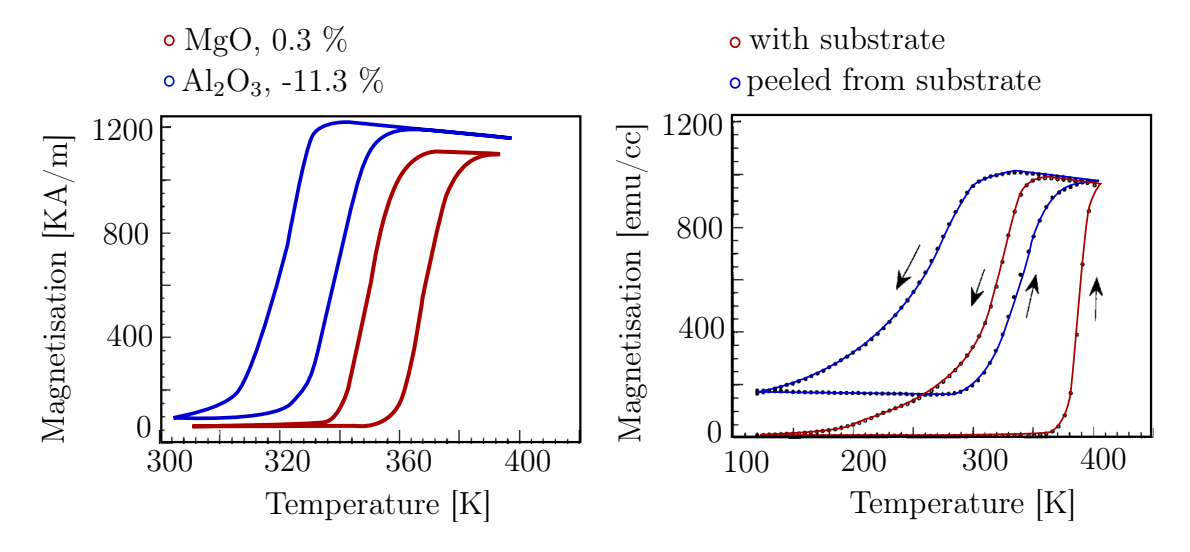


Figure 2.5: The left graph displays the magnetization curve of FeRh on Al_2O_3 with a misfit parameter of -11.3% and on an MgO substrate with a smaller compressive substrate strain of 0.3%. The right graph displays the influence of the MgO substrate. Adapted from [40] and [41].

These shifts in phase transition temperature occur due to strain, caused by lattice mismatch between the film and its substrate created either during film growth or from thermal expansion. Misfit parameter f_m , sometimes also called epitaxial strain ϵ , can be calculated as:

$$f_m = \frac{a - a_s}{a_s}. (2.3)$$

For FeRh, the lattice is positioned on the MgO substrate, as illustrated in Figure 2.6. To obtain the misfit parameter $f_m = 0.3\%$, we substitute $a_{\text{FeRh}} = 2.987 \text{ Å}$ and $a_{\text{MgO}} = \frac{\sqrt{2}}{2} \cdot 4.216 \text{ Å} \approx 2.978 \text{ Å}$.

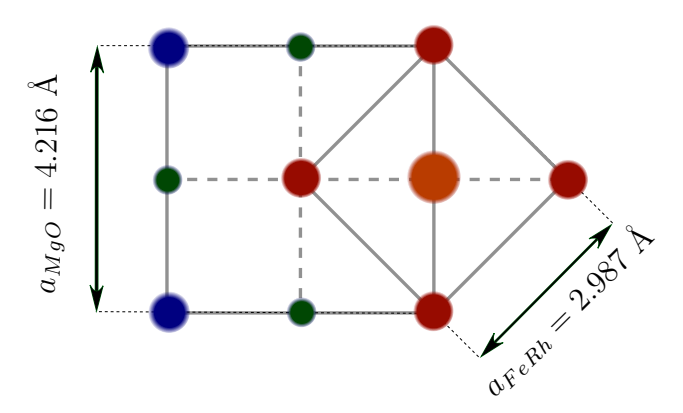


Figure 2.6: Crystal lattice alignment of FeRh during epitaxial growth on an MgO substrate. Adapted from [18].

This compressive strain prevents the lattice parameter from expanding, thereby inhibiting phase transition and increasing the transition temperature T_p . If we peel the film from the substrate or create patterned structures, we allow the material expansion and release the stress, which leads to decrease of the T_p . The space for material expansion is also created in patterned thin films, which could lead to different transition temperatures for patterned and non-patterned layers.

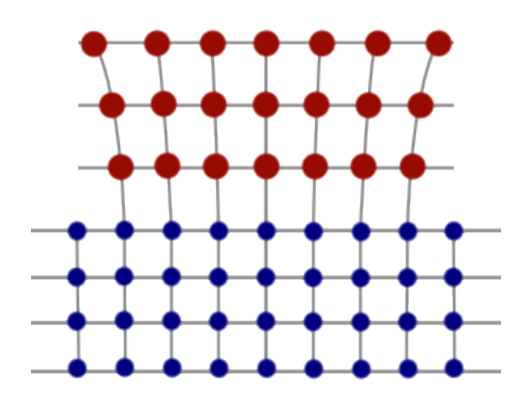


Figure 2.7: Relaxation of compressive strain caused by substrate. Adapted from [42].

2.3 State of the art

Our aim is to use strain relaxation in the structured films to create a phase interface between ferromagnetic structure (wire) with relaxed strain and full strained antiferromagnetic film. Because this interface is influenced by many factors, we are interested in the process of phase domain formation and domain structure at different depths below the film surface. In this section we present interesting papers, that can help us choose appropriate structure shapes, thicknesses and to clarify ambiguities related to the transition.

2.3.1 Nucleation of phase domains

The formation of domains in the full film varies in domain size and direction of nucleation. An important fact is, that repeated heating and cooling preserves the positions and shapes of the domains. In the article [43] authors observed formation and dissolution of ferromagnetic domains on samples deposited by magnetron sputtering under various growth conditions, with varied power and annealing times. The increase of the annealing time shifts the transition temperature to higher values. Changing the power at a constant deposition time of 7 minutes will affect the concentration of Rh atoms and the film thickness. Rhodium atoms in comparison to iron are better deposited at high power, since they have higher mass and need higher kinetic energy during the deposition. The thickness linearly increases with power. The applied power range 50-230 W corresponds to the thicknesses 90-180 nm.

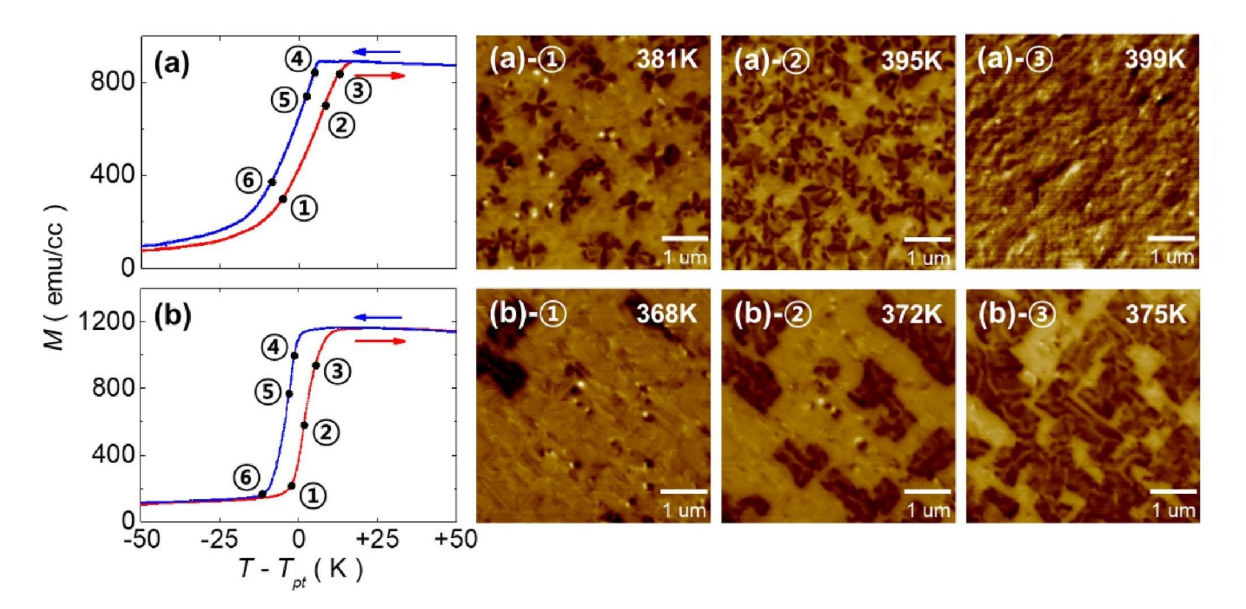


Figure 2.8: Temperature-dependent magnetization of FeRh films grown under sputtering powers of (a) 60 W and (b) 130 W, with $T_p = 383$ K and 370 K, respectively. The right panels display magnetic images taken using MFM during heating. Taken from [43].

In the picture 2.8(a), the power 60 W corresponds to FeRh layer about 95 nm thick. The FM domains are nucleated randomly with inhomogeneous shapes and the density of nucleation sites is quite high. On the other hand in Figure 2.8(b) a 130 nm film shows less nucleation areas and bigger domains of rectangular shape strongly dependent on direction. According to [43], the preferred nucleation direction is along (100).

A Master's thesis [44] also deals with the formation of phase domains for two FeRh samples, again grown by magnetron deposition. The author compares the phase domains for the 200 nm and 36 nm thick films shown in Figure 2.9. After comparing the phase domains for both thicknesses, we reach the same conclusions as the previous mentioned article. The domains on the thinner layer have significantly smaller dimensions and their nucleation is not dominant in any directions. On the contrary, the domains on the 200 nm thick layer are larger and oriented along two perpendicular axes. Author

of the thesis calculated the domain size using Height-Height Correlation Function. The correlation length for maximal phase separation during the cooling is (299 ± 3) nm and during the heating (248 ± 6) nm for a film with 200 nm thickness. For the thinner film of 36 nm the correlation length for maximal phase separation during heating was lower (155 ± 3) nm.

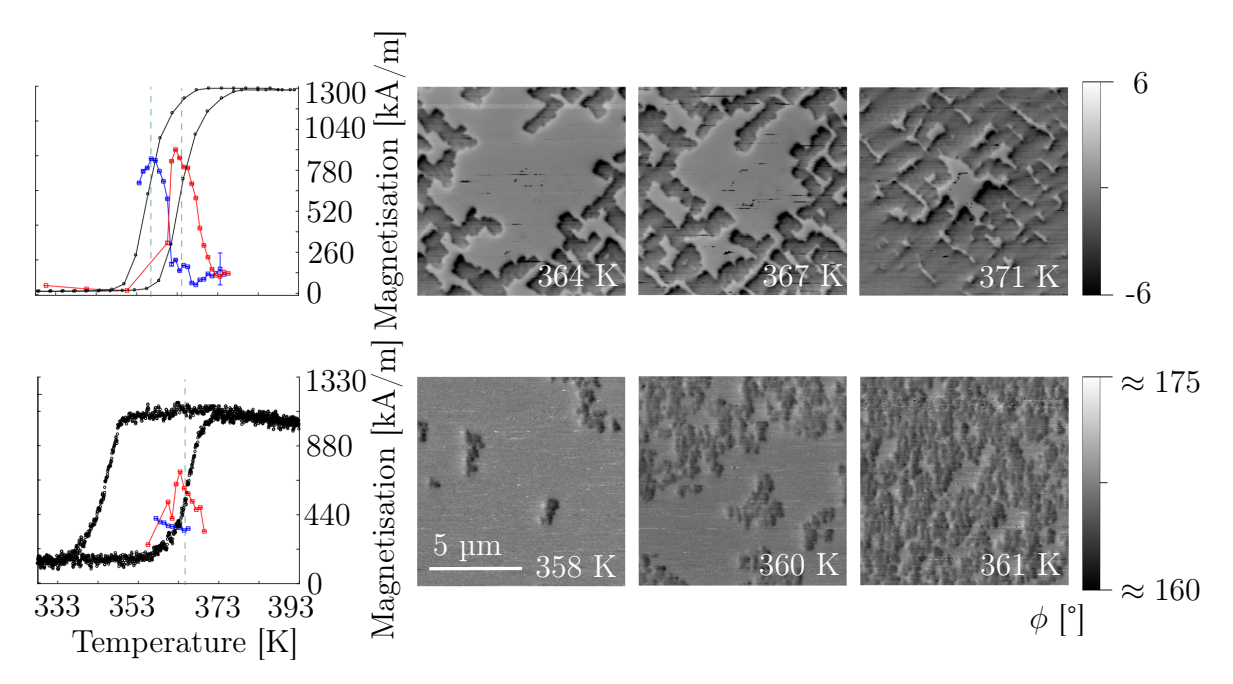


Figure 2.9: Temperature-dependent magnetization of FeRh films with thicknesses 180 nm (upper row) and 36 nm (bottom row). The right panels display magnetic images taken using MFM during heating. Adapted from [44].

In the section 2.2 we mentioned the influence of epitaxial strain on the phase transition temperature. This strain may also be responsible for the significant anisotropy of the domains nucleation. As the energy of the strain increases linearly with film thickness, the nucleation anisotropy is more pronounced in these films than in thinner films.

A paper [45], focused on free energy calculations, presents MFM images for 20 nm and 50 nm thick layers on five different substrates causing compressive strain from 0.3 to 12 %. For FeRh on MgO, both 20 nm and 50 nm layers contain small phase domains challenging the MFM image resolution limits. The thicker film shows more distinct phase domain clusters and greater phase signal contrast compared to the thinner FeRh layer.

Another unknown is how the domains form within the film. It is not clear whether nucleation occurs from the substrate, from the top layers or randomly. This issue was dealt with in the article [46], which examined very thin layers (up to 10 nm) and concluded that 1.5 nm thick AF layer appears between the FM phase and the substrate. The paper [47] examined a thicker layer (56 nm) and concluded, through calculations and time dependencies of the magnetization measurements, that domains first form on the surface of the layer and then gradually penetrate into the film.

An asymmetry of the FM-AF transition during cooling and AF-FM during heating

is often demonstrated. Article [48] concludes that the formation of AF phase during cooling is dominated by nucleation at defects, whereas upon heating the heterogeneous nucleation in various places is observed. This results in the AF phase having a small and non-random final domain structure and the FM phase having a significant increase in domain size. This statement is supported by the results of the thesis [44] that reported different values of the FM domains for cooling and heating for a 200 nm thick FeRh layer.

2.3.2 Phase domains in patterned films

Spatial constraints have a significant effect on the properties and behaviour of the sample. Thus, we mention a few findings from papers dealing with structured FeRh thin films.

The first paper we mention is [49], which observed a step change in resistance dependent on temperature for FeRh strips formed by lithography on a magnetron-sputtered layer. These discrete jumps were especially pronounced during cooling of the sample, rather than during heating, indicating a significant asymmetry between the heating and cooling processes. The measurements showed a gradual formation of FM domains during heating and a stepwise nucleation of AF domains during cooling.

Measurements were conducted on three samples. The first sample, with a film thickness of t=25 nm and stripe width d=1100 nm, did not exhibit this behavior and showed symmetrical resistance dependence for both heating and cooling. In the second sample, with t=33 nm and d=550 nm, a noticeable but still not significant asymmetry was observed. The phenomenon was most pronounced in the third sample, where t=50 nm and d=220 nm.

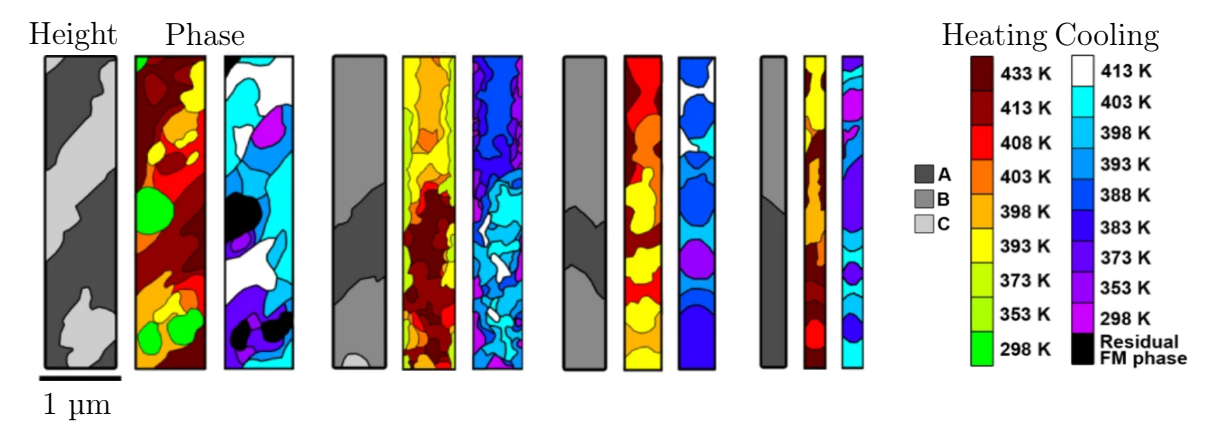


Figure 2.10: Lithographically formed wires on a 50 nm thick FeRh film that are 0.75, 0.5, 0.35 and 0.2 μm wide respectively. Adapted from [34].

From MFM measurements of 50 nm thick layer containing wires with different widths from paper [34] in the Figure 2.10, we can observe, that at the 500 nm wide wire, the FM phase is more stable at the edges of the wire. This behaviour is expected due to strain relaxation. At wire with even smaller widths, FM phase strips are formed between the edges of the wire especially during cooling.

Supercooling is an effect that allows a phase to occur even below the transformation temperature. It is mainly observed in chemically pure materials with a small number of defects that could potentially become nucleation centres. In the aforementioned thesis [44], this effect was observed on on discs with 700 nm and 500 nm diameter. The lithographic patterns on an epitaxial 36 nm thick FeRh layer showed FM phase during cooling even at temperature 302 K (Figure 2.11). The measurements comprised three scenarios. In the first, there was a gradual transformation of the disk with more nucleation centres (yellow label in picture 2.11), in the second, the disc transformed rapidly with no centres detected (red label), and in the third, there was no transformation of the disk at all. The disks were enclosed by a frame, about 500 nm wide, which, although converted earlier compared to the disks, also experienced significant supercooling (blue elipse).

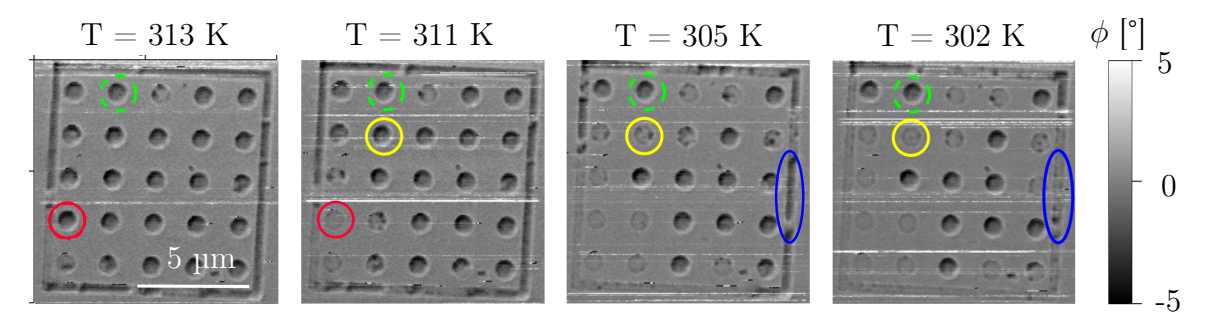


Figure 2.11: Supercooling of 700 nm disks on a 36 nm thick layer. Taken from [44].

From the preceding paper research, we can conclude following statements:

- The thicker layer provides larger domains, with reduced number of nucleation centres and more pronounced anisotropy of nucleation.
- The precise domain structure at different depths remain unknown. According to [47], the domain nucleation begins at the surface in 50 nm thick FeRh layer.
- Asymetry in heating and cooling might appear during domain formation. In structured films asymmetry in resistance measurements was also observed.
- Small structures (like disks with diameter up to 1 µm and wires with width up to 1 µm) can be supercooled by tens of Kelvins.
- On wires with width below 1 μm is the FM phase more stable at the edges. For strips with a radius of 500 nm or less, a step transition could occur.

3. Experimental techniques

3.1 Magnetron sputtering

Magnetron sputtering is a physical vapor deposition (PVD) technique employed to create thin films from a wide range of materials including metals, ceramics and polymers. The underlying principle is the sputtering of the deposited material (target) with heavy atoms such as Ar. The chamber is composed of a target, above which the substrate and anode are placed. Below the target is a cathode and coils that create a magnetic field trapping electrons. The electrons move over the target trapped in a magnetic field. When injecting the Ar atoms into the chamber, the electrons collide with them, forming cations Ar⁺. Cations creating plasma gas are accelerated towards the target by the cathode. Collisions between the target and the ions result in the sputtering of the material. If the material reaches the substrate, it adheres and is successfully deposited. To ensure uniform deposition the sample holder rotates with the sample.

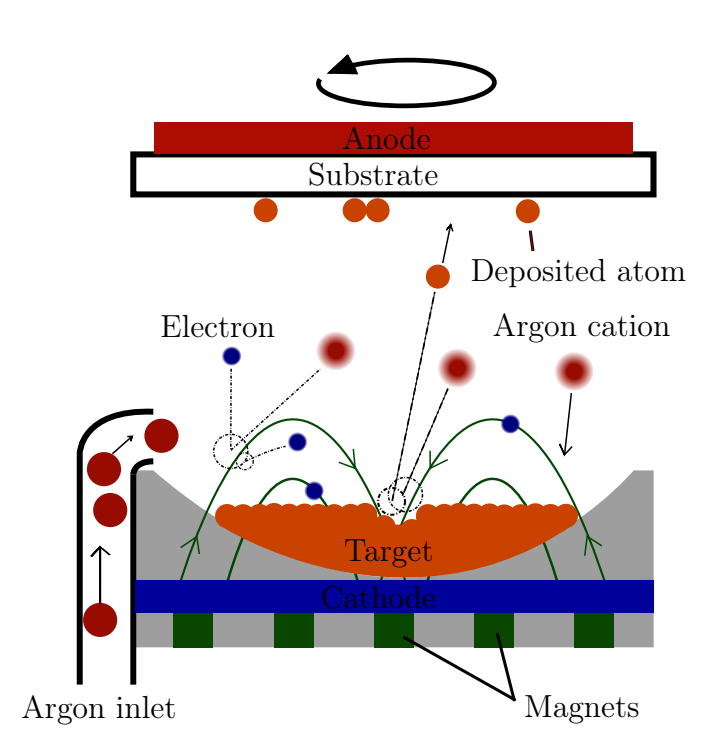


Figure 3.1: Magnetron sputtering process. Adapted from [50].

Thin film deposition of FeRh was performed on magnetron sputtering system BESTEC at CEITEC. This system contains load lock and main chamber to secure UHV (Ultra

High Vacuum). Sample holder enables heating up to 1100 °C, which is important in three phases. First phase is preheating the substrate to reduce impurities and contamination on the surface. Second phase is heating during deposition to increase atom diffusion to achieve layer by layer growth regime. The third phase is annealing after deposition, that is crucial for reducing the film stress and obtaining appropriate lattice structure [50].

The parameters we use to control the thickness are deposition rate and deposition time. The crystal structure is influenced by the deposition temperature and the annealing temperature and time.

3.2 Vibrating Sample Magnetometry

Vibrating sample magnetometry (VSM) is a technique employed to assess the magnetic properties of materials. The sample is positioned within the magnetic field of an electromagnet between two detection coils. Vibration alters the flow of the magnetic field through the coils, inducing the voltage that is being measured. VSM enables the determination of the magnetic properties of the sample, including magnetic susceptibility, coercivity and magnetic remanence, as a function of temperature or magnetic field. In the course of our experiments, we employ the external field solely for the purpose of orienting the magnetic moments of the ferromagnetic phase domains. We will subsequently measure the magnetisation of the sample as a function of temperature. The resulting curve represents the average of the magnetic properties of the smaller regions of the sample. The measurements were again performed on a VersaLab vibrating magnetometer at CEITEC Nano.

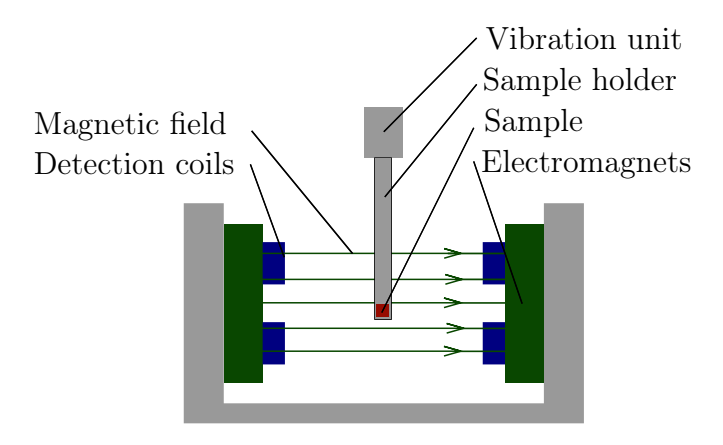


Figure 3.2: Schematic diagram of a vibrating sample magnetometer. Adapted from [51].

3.3 Atomic Force Microscopy

Atomic force microscopy (AFM) is a technique providing detailed information of the surface topography with nanometre resolution. The AFM operation principle is the using a very sharp tip (probe) that is driven over the sample surface and responds to the interaction force between the tip and the atomic structures on the surface.

There are several basic modes of operation. One is a contact mode, in which the tip mechanically scans over the surface, and the inclination of the cantilever is used to record the force between the tip and the sample. Another is a tapping mode, in which the oscillation of the probe is excited. As the oscillating probe scans over the surface, the phase and amplitude of the oscillation are changed depending on the distance between the sample and the tip. Both of these modes offer additional regimes. In the contact mode, these are the constant height regime, where the change in force is recorded, and the constant force regime, where the topography is obtained from the scanner signal in the z-axis. The tapping mode regimes are amplitude modulation or frequency modulation and their description is shown in the Figure 3.3.

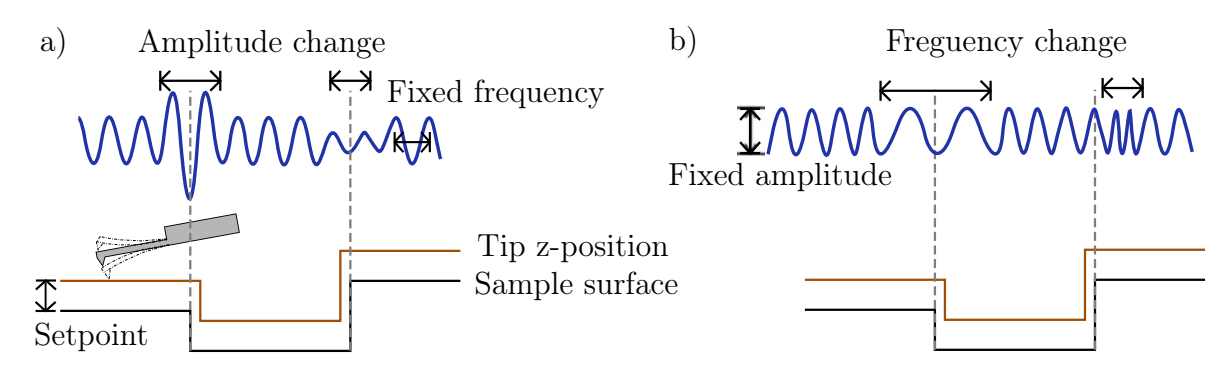


Figure 3.3: a) Amplitude and b) Frequency modulation regimes. Adapted from [52].

The AFM probe is typically composed of a sharp tip and a cantilever. The spring constant of the probe is dependent on the material (typically silicon or silicon nitride) and the dimensions of the cantilever (width, thickness and length). Its value affects the resonant frequency of the probe for dynamic (tapping mode) modes. The tip radius significantly limits the resolution of the whole microscope and therefore efforts are made to minimise its dimensions. The aforementioned probe parameters are usually specified by the probe manufacturers.

The probe is placed in a holder that employs piezoelectric motors to scan and move on the sample. Cantilever deflection is most often detected by a laser reflecting off the cantilever. However, an alternative approach may be using self-sensing probes that do not utilise any optical or mechanical detection systems. The sensing of the interaction between the tip and the sample surface is conducted electrically.

In order to mitigate the effects of high noise levels, a Lock-In amplifier is incorporated into the circuit. This device employs a reference signal to select the most appropriate frequencies from the measured signal and thus reduces the impact of noise.

Feedback is also an essential component, which we will demonstrate with the example of contact mode measurement in constant force mode. Sensors located near the probe tip continuously monitor the interaction force between the probe tip and the sample surface. The measured interaction force is compared to a setpoint (SP) that is determined by the user, for example a constant force value that they want to maintain. Based on the difference between the measured value and the SP, the position of the probe is controlled. If the interaction force is higher than the SP, the system will reduce the distance between the probe tip and the sample surface. The probe moves

above the sample surface and is controlled to maintain a constant interaction force. During this process, the measured probe positions are used to create an image of the surface topography. SP determines how much power we want to maintain. A high SP allows for greater resolution, but this is at the risk of damaging the tip and the sample. Control of the feedback loop is done through the proportional-integral-derivative (PID) regulator [53].

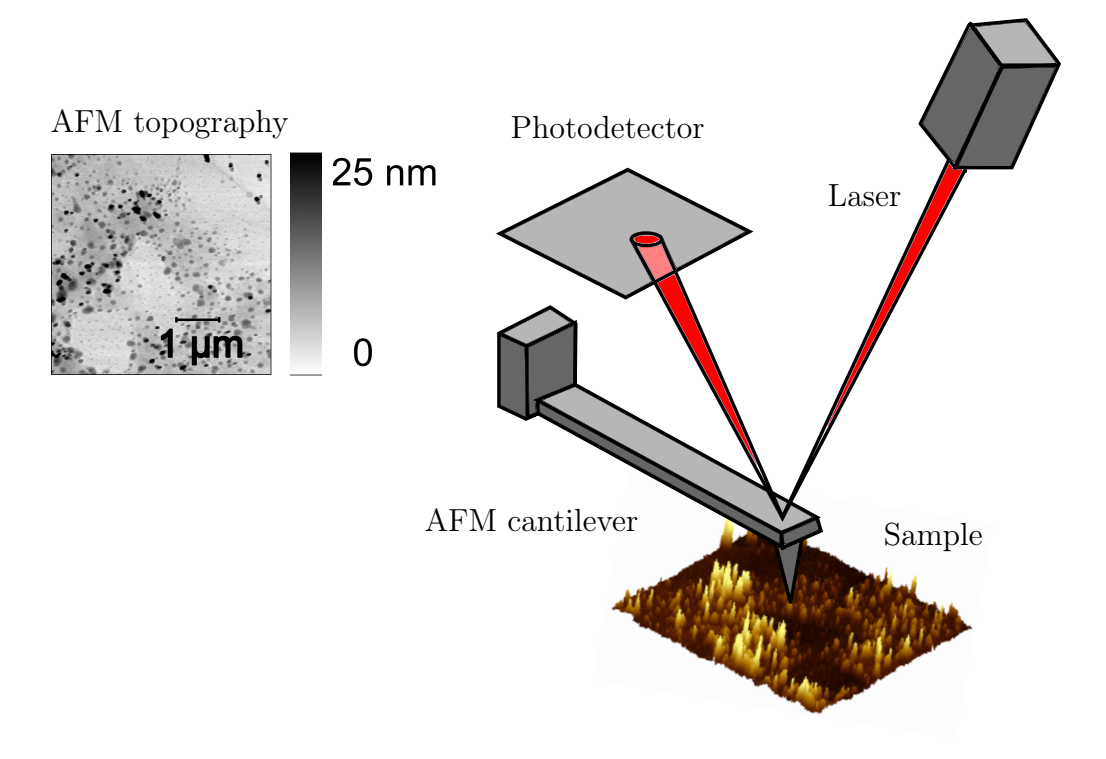


Figure 3.4: Schematic of the AFM scanning setup [54].

3.4 Magnetic force microscopy (MFM)

Magnetic force microscopy is a specialized variant of AFM that focuses on imaging the magnetic properties of materials at the microscopic and nanoscopic level.

MFM operates in amplitude modulation mode, a dynamic force mode where the tip maintains oscillation at a constant resonant frequency. In dual-pass mode, the MFM tip first scans the sample topography to create a surface map. Then, it lifts by a defined lift height and scans above the surface again. During this second pass, the tip records phase changes corresponding to gradient of stray field. Small lift height values lead to better resolution, but they entail the potential for damage to both the tip and sample due to collision. Increasing the lift height can help with topography interference in the magnetic signal, but at the cost of reduced contrast and resolution. The repulsive magnetic force gradient shifts the resonance curve to a higher frequency, accompanied by an increase in phase shift, resulting in bright contrast. Conversely, an attractive force leads to dark contrast. It is therefore essential to use a tip with either a magnetic coating or one made entirely of magnetic material when performing MFM measurements. This method effectively utilises the long-range nature of magnetic

forces, contrasting with the short-range forces caused by atomic interactions.

The AFM and MFM measurements presented in this work were conducted at the CEITEC Nano research infrastructure on ICON microscope from Bruker Corporation. MESP probes, manufactured by this company and comprising a hard cobalt-chromium coating, were employed for data acquisition. These probes exhibit a resonant frequency of 75 kHz and a spring constant of $3~\rm N/m$.

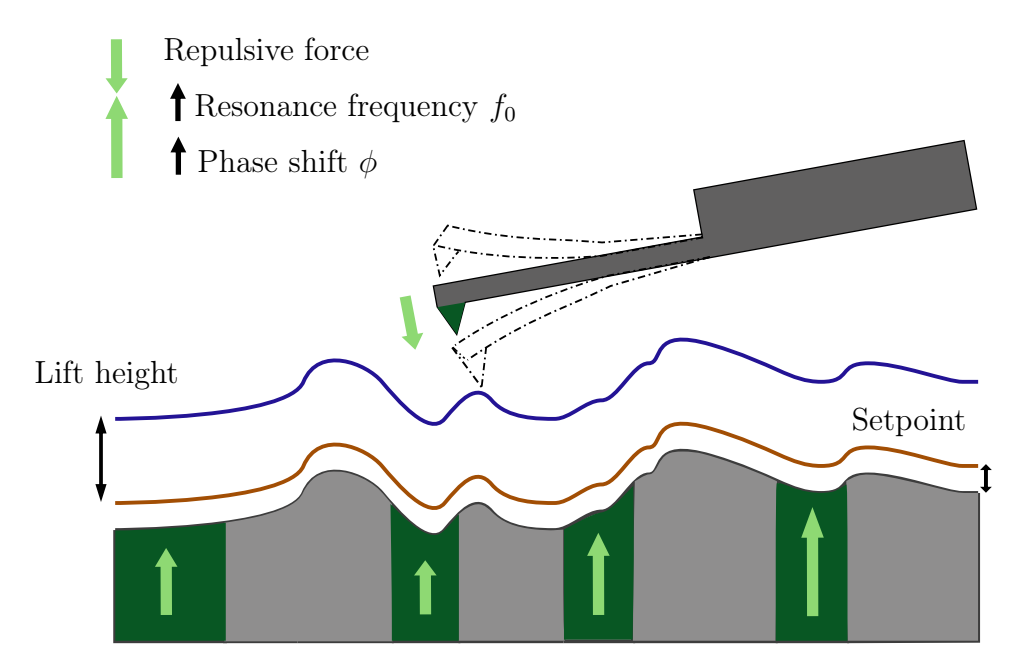


Figure 3.5: Magnetic force microscopy measurement process [52].

4. Sample Characterisation

FeRh layers of 36 nm and 180 nm thicknesses were deposited on MgO substrates. The MgO substrates used for FeRh thin films had a crystalline orientation of (001) and dimensions of 5×5 mm² and were chosen for their lattice compatibility with FeRh, which is crucial for promoting epitaxial growth and achieving high quality layers. Post-deposition, the FeRh layers were patterned using electron beam lithography into stripes of varying dimensions connected to pads at one or both ends. The existence of the lateral phase interface is expected due to different strain conditions within the pad and the stripe. The strain can be influenced primarily by the dimensions of the stripe and also its orientation with respect to the substrate (001) crystal orientation. For this reason, several structures containing strips with widths ranging from 200 nm to 2000 nm, lengths from 1 µm to 25 µm, and various orientations were fabricated on both samples. Examples of different structures is shown in the Figure 4.1 below.

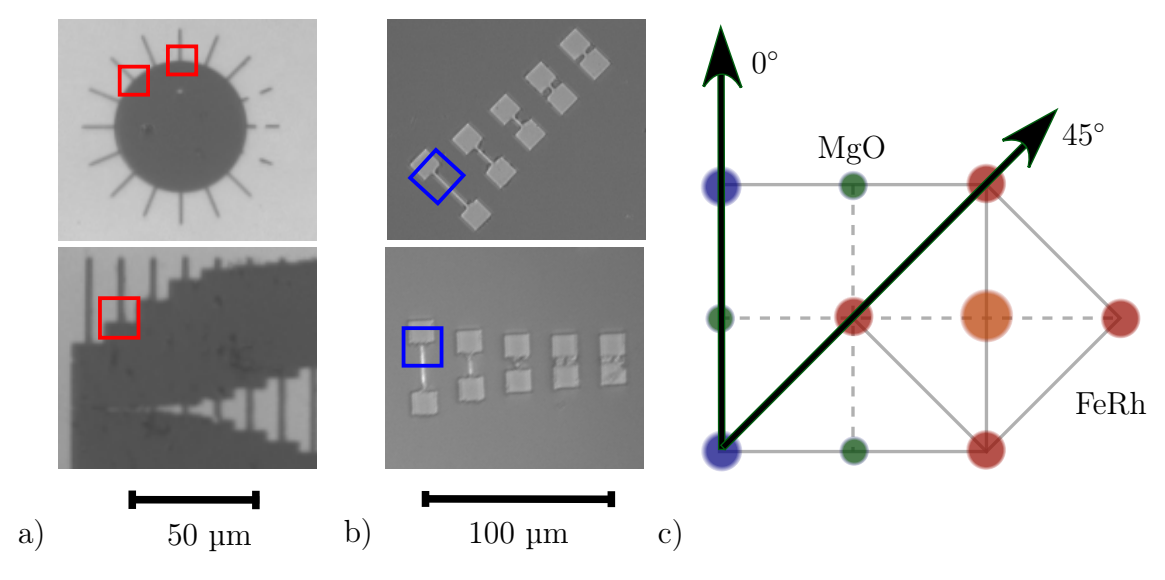


Figure 4.1: (a) Structures fabricated on a 36 nm thick film. The red areas show the regions characterized by MFM. For the upper sun-shaped structure, we focused on the 0° and 45° orientations. For the lower structure, we focused on the wire connected to the structure at one end only. (b) Structures on the 180 nm thick layer were composed of wires always connected to the pad at both ends. The top structures have the wire at a 45° angle to the substrate. The lower structures have a 0° angle. Blue squares indicate examples of areas characterized by MFM. (c) Representation of the 0° and 45° angles of the wire with respect to the substrate.

The FeRh layers were deposited using Magnetron sputtering together with M.Sc. Jon

Ander Arregi Uribeetxebarria, Ph.D. During the deposition, the substrates were kept at a temperature of 400°C for a duration of 100 minutes. This temperature was chosen to ensure that the Fe and Rh atoms have sufficient mobility to arrange into the desired CsCl-type ordered structure. Achieving this specific atomic ordering is essential for the material to exhibit the desired AF-FM transition. If the deposition temperature were too low, the atoms would not have enough energy to reach their correct positions, potentially resulting in an unwanted FM face-centered cubic structure. Conversely, high temperature could cause the formation of dewetted areas due to interplay between epitaxy and surface tension.

After deposition, the samples were annealed for 90 minutes at 615°C. This annealing step further assists in achieving the correct atomic ordering and relieving any internal stresses that might have developed during the deposition.

The lithography process carried out by my supervisor, Ing. Oleksii Zadorozhnii, was different for the two samples. The first sample, with a 36 nm thick FeRh layer, was fabricated by negative lithography without lift-off. The second sample was fabricated using positive lithography with two PMMA (polymethyl methacrylate) resists layers. After applying the PMMA layers and Electra, Titanium (Ti) was deposited using Physical Vapour Deposition, which was then acting as a hard mask for Ar etching of FeRh film. Wet etching in Buffered Oxide Etch was used to get rid of the remnants of the mask after the etching processes.

4.1 Sample with 36 nm thick FeRh layer

During the first measurements, we selected wires with the smallest fabricated widths: 1000 nm and 1500 nm with 0° orientation relative to the MgO (001) lattice.

Strain relaxation influence was significantly visible at the edges of the narrowest 1000 nm wide wire in the Figure 4.2, prompting a detailed focus on these narrower structures. Despite the film thickness being only 36 nm, the structures' height reached approximately 100 nm due to overetching during lithography. Consequently, a lift height of 100 nm was chosen for the magnetic measurements to accommodate this.

At room temperature, the sample predominantly remains in the AF state with a minor FM residue on the wire. The bright contrast observed at the edges of the structure is an artifact of the topographical changes rather than the origin of magnetic forces. The prominent negative signal in the upper right corner is similarly non-magnetic.

Even though the phase domains are very small, we can observe larger domain clusters and also change of contrast indicating the phase domain behavior. These clusters suggest a clear distribution of stress influenced by the substrate or intrinsic defects, aligning well with our expectations.

During cooling the first clusters start to appear in the pad around the temperature $117~^{\circ}$ C, indicating the onset of the phase transition from FM to AF. Around $87~^{\circ}$ C a gradual transformation also becomes visible in the wire. The FM phase persists in the wire and at the edge of the structure, where it remains abundant even at $57~^{\circ}$ C.

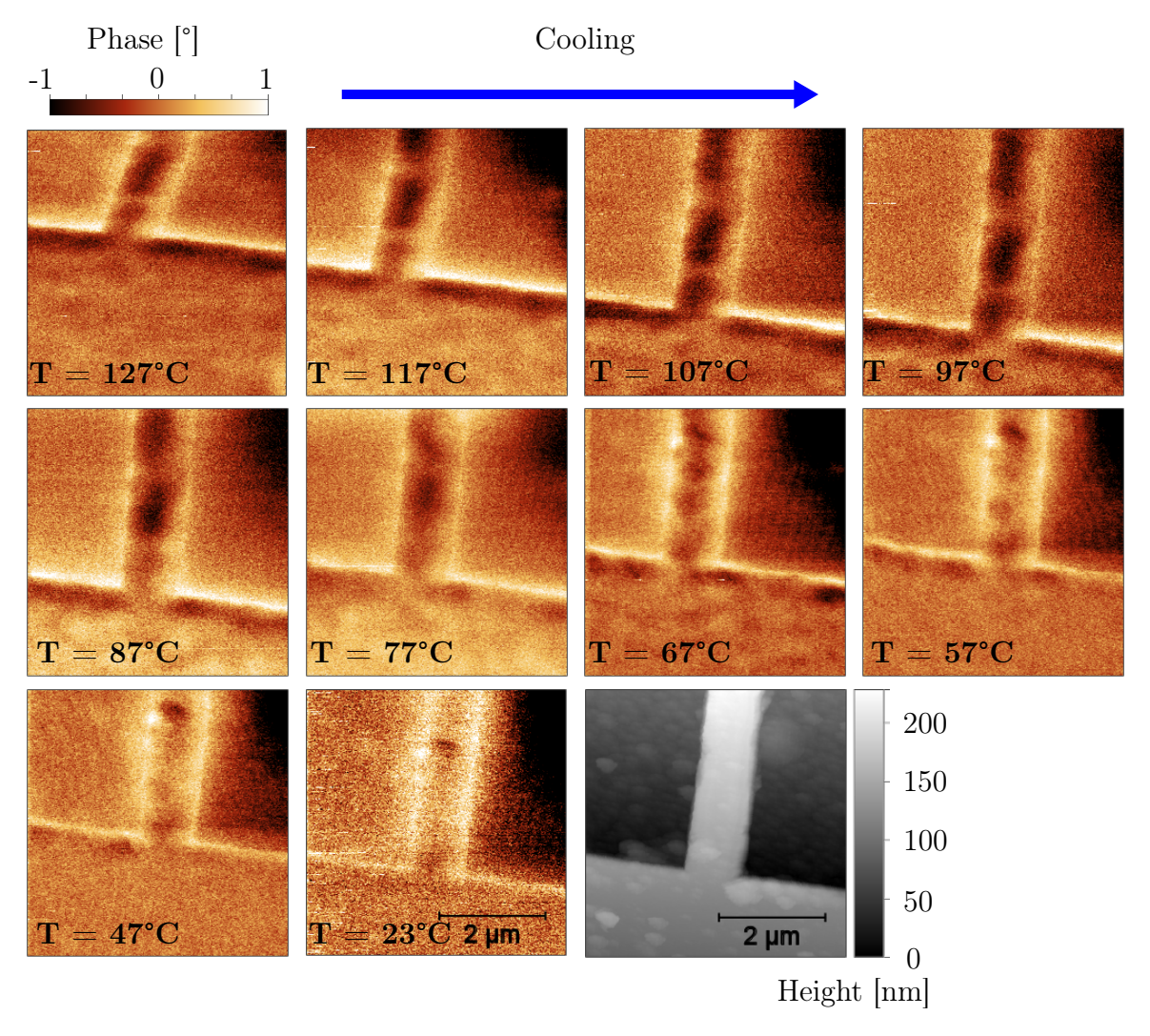


Figure 4.2: Phase transformation from FM to AF order during cooling of a 1000 nm wide, $25 \mu m$ long wire with 0° orientation relative to the substrate, which is perpendicularly bonded to a continuous layer on a $36 \mu m$ thick FeRh film.

The strain relaxation of the FeRh crystal structure varies for different epitaxial directions. When the orientation of the stripe is 0° with respect to the substrate (as we can see in the Figure 4.1), its expansion at the edges is in the crystallographic direction (110), and when the orientation is 45°, it is in the direction (100). Since the stripe has less material surrounding it, it experiences a larger degree of strain relaxation compared to the film. That is the reason why on Figure 4.2 we see a difference in phase transition temperature between the stripe and the film.

Wires 1000 nm wide with orientation 45° relative to the substrate show much weaker strain relaxation effects, since in the Figure 4.3 the only sign of the relaxation is a weak remanent FM phase at the edges.

However, the comparison of these two measurements (in the figures 4.2 and 4.3) is not conclusive enough, as it was made on two different structures under different conditions. For this reason we repeated the measurements under the same conditions on an identical structure shown in the Figure 4.4, where the 0° orientation has a much more pronounced remanent FM phase at the edges than the 45°, which confirms our

assumptions.

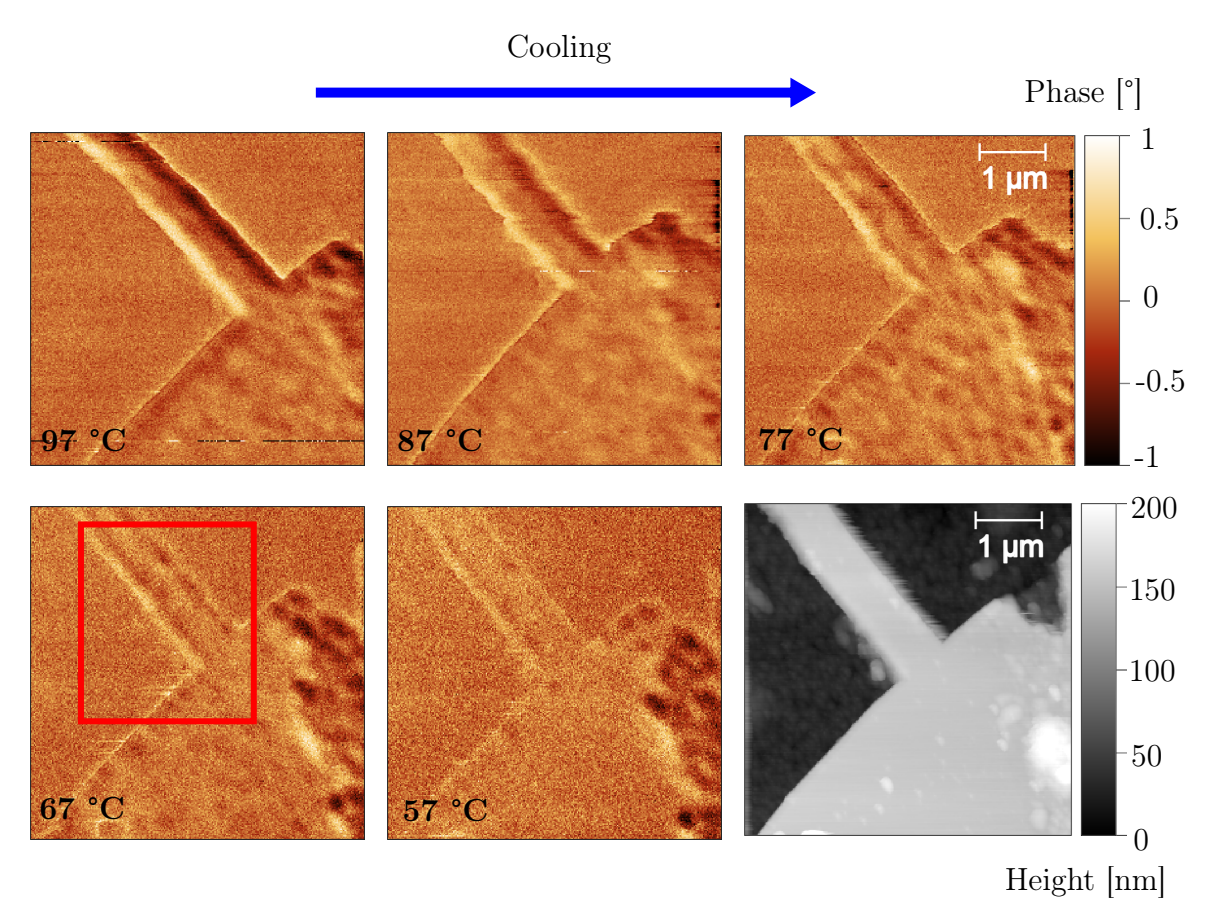


Figure 4.3: Phase transformation from FM to AF order during cooling of a 1000 nm wide, 12 µm long wire with 45° orientation relative to the substrate, which is perpendicularly bonded to a continuous layer on a 36 nm thick FeRh film. The red frame highlights the remanent FM phase at the edge of the sample.

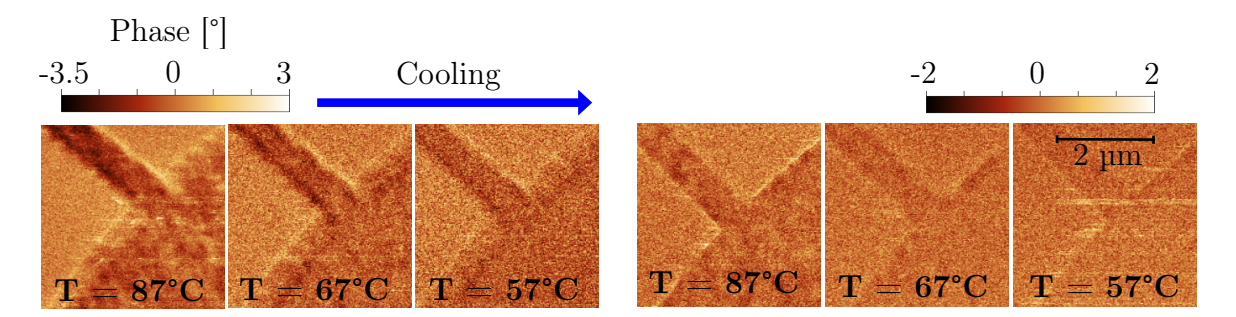


Figure 4.4: Comparison of 1000 nm wide wires connected to the same sun-shaped structure measured with similar probe under the same MFM conditions. The wire with the 0° orientation (shown on the left) shows more FM phase at the edges of the structure than the wire oriented 45° (right), and the FM phase also remains at lower temperatures.

4.2 Sample with 180 nm thick FeRh layer

To investigate the nature of domain nucleation, we first characterized the 180 nm thick layer prior to lithography. During heating, we observed domain nucleation and documented the entire temperature dependence of the magnetization. MFM measurements were performed around the dewetted regions, which had an area on the order of microns and a depth of approximately 50 nm. These regions induce compressive stress and showed no FM signal in our measurements.

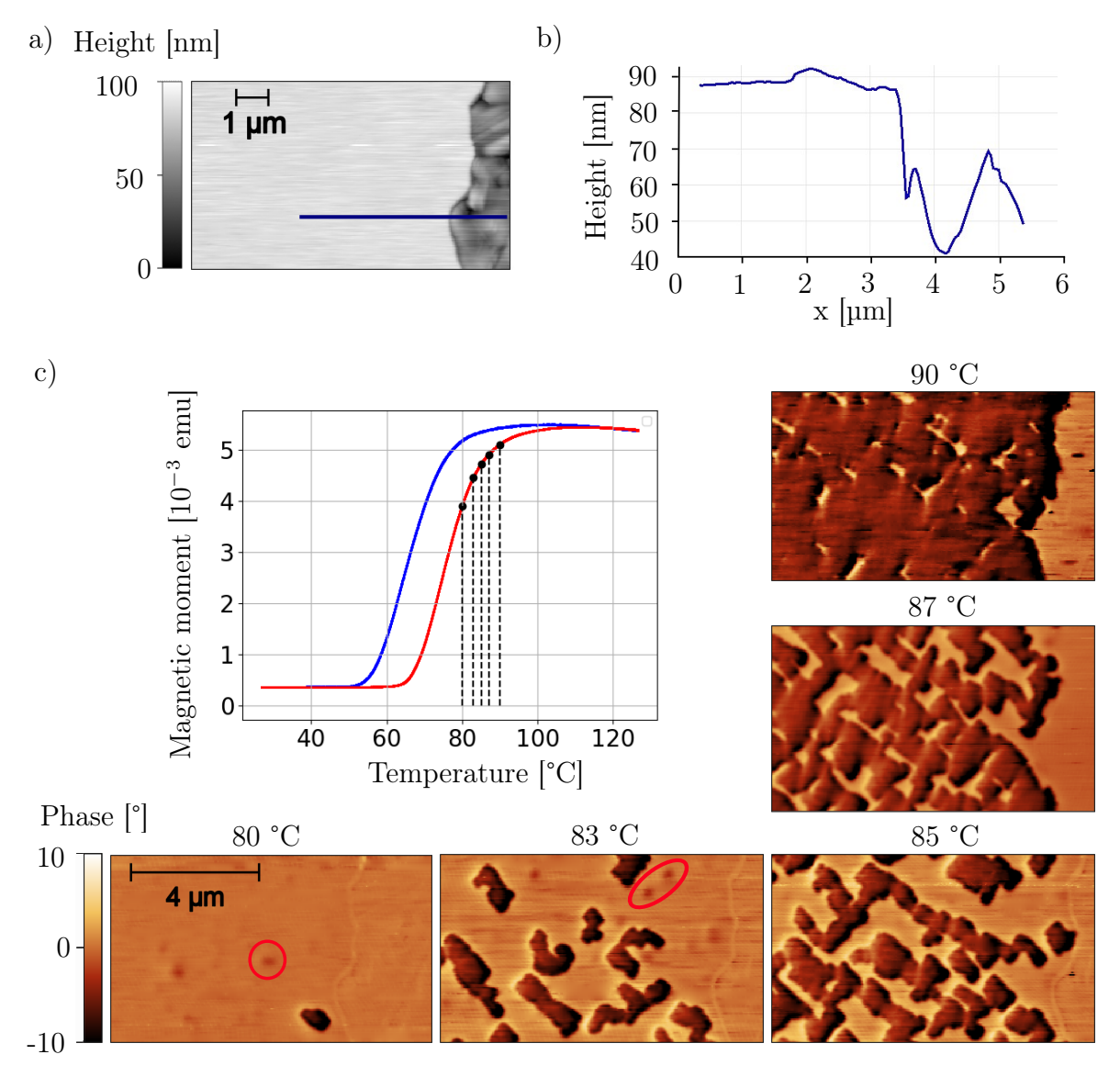


Figure 4.5: Characterisation of the 180 nm layer of FeRh. a) Topography of the surface, which contains a dewetted area on the right-hand side. b) Height profile from the location shown in the topography image. The sample surface around the dewetted area with a depth of 50 nm contains only small irregularities. c) VSM characterisation of the sample with the temperature points at which the MFM scans were performed marked. The MFM scans show the gradual formation of domains around 1 µm in size. The red areas highlight domains with weaker signal. These may either be domains with smaller dimensions or sub-surface domains.

The flat surface allowed for a low lift height and a small amplitude setpoint. Combined with the strong signal from the larger, more easily measurable domains, this setup provided high-quality images.

The VSM data revealed that the transition occurs between 50 °C and 100 °C. The point where the curves have the largest gradient is called the transition temperature. The value of the transition temperature during heating is 75 °C, and during cooling, it is 64 °C. The phase domains were observed to be regular and directionally dependent, reflecting the stress distribution and the interplay between expanding lattice of the FM domains and the compressive strain of the surrounding material.

To determine the shape of the interface, it is important to examine not only the phase domain shapes on the sample's surface but also the behavior of the domains throughout the entire layer thickness. The magnetic domains, marked red in Figure 4.5, exhibit significantly weaker intensity and smaller size, suggesting that these domains may be located beneath the sample surface.

Patterned structures

The Figure 4.1 displays four variations of wires and connected to surfaces, which were created by the electron beam lithography on the previously described continuous layer. The sample contains wires with widths ranging from 200 nm to 2000 nm and lengths from 1 µm to 25 µm. Wires wider than 800 nm have a flat surface and their widths correspond to the desired specifications. In contrast, wires narrower than 600 nm exhibit a triangular profile, with their base width generally exceeding the intended dimensions.

Table 4.1: The state of wires with various widths and orientations according to the substrate at temperatures 63 °C and 54 °C.

Wire width [nm]:	2000	1250	800	600	300
$T = 63 ^{\circ}\text{C}, 0^{\circ}$	AF	AF/FM	FM		
$T = 63 ^{\circ}C, 0^{\circ}$	FM	FM	FM	FM	
$T=54^{\circ}C,0^{\circ}$		AF	AF/FM	AF/FM	
$T=63^{\circ}C,45^{\circ}$		FM	FM	FM	
$T=54^{\circ}C,45^{\circ}$		AF	AF	AF	AF

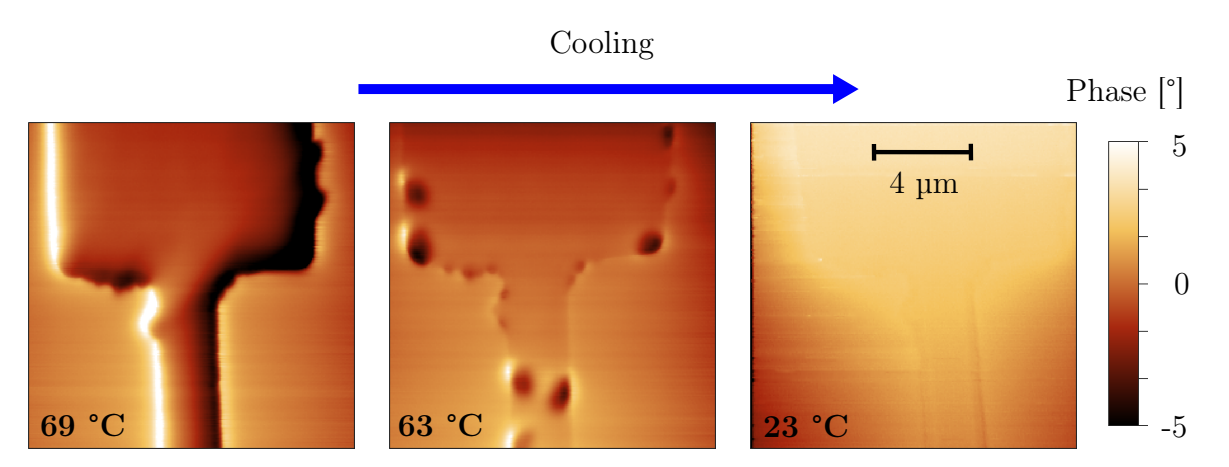


Figure 4.6: An example of a 2000 nm thick wire transformation, during which no phase interface was formed, the transformation of the film including the wire occurred in a stepwise manner. After this transformation, only a few FM domains remained, which disappeared with gradually decreasing temperature.

Table 4.1 compares the state of wires of different thicknesses at a specific temperature. Whenever phase coexistence occurred, the FM phase was always present on the wire and AF phase on the pad as desired. For wires oriented at 0°, coexistence was observed in stripes smaller than 1250 nm. In contrast, for wires oriented at 45° degrees relative to the substrate, the effect of stress relaxation, as seen in the thinner 36 nm layer, was less pronounced, and no phase coexistence was observed even for 300 nm wide wires.

Another observation from Table 4.1 is that the transformations occur within the temperature range of 63 °C to 54 °C. To investigate further, we measured the state of the wire and pad in 3 °C increments within this range. Specifically, we examined three 1000 nm wide wires with orientations of 0° and 45°, as well as shorter lengths. Table 4.2 shows that phase coexistence does not occur for wires with a 45° orientation or for shorter wire lengths.

Table 4.2: The state of the 1000 nm wide wires with various lengths (25, 20, 8 μm) and orientations according to the substrate (0°, 45°) during the gradual cooling.

Temperature [°C]:	70	67	64	61	58	55	52	49
1000 nm, 0°, 25 μm	FM	FM	FM	FM	AF/FM	AF	AF	AF
1000 nm, $45^{\circ},25~\mu m$	FM	FM	FM	FM	FM	AF	AF	AF
$1000 \text{ nm}, 0^{\circ}, 10 \mu\text{m}$	FM	FM	FM	FM	FM	FM	FM	AF
$1000 \text{ nm}, 0^{\circ}, 8 \mu\text{m}$	FM	FM	FM	FM	FM	FM	FM	AF

During both measurements in tables 4.1 and 4.2, a step transition from the FM to the AF phase of the pads was observed. This phenomenon was confirmed using a Kerr microscope during cooling of the sample, where the change in light reflection was recorded as a function of the magnetic properties of the material, since AF phase of FeRh has higher reflectivity than the FM phase. As a result, the transformation of the material from FM to AF phase led to the brightening of the pad. The temperature at which the pad transitioned showed no dependence on the wire dimensions. Addi-

tionally, in most of the cases, the pads connected by the same wire have transformed independently, but occasionally the transformation was also simultaneous.

During cooling of the structure with the $1 \times 25 \,\mu\text{m}^2$ wire shown in the Figure 4.7, a stepwise transformation of the pad was observed, while the wire remained in the FM phase. As cooling continued, the FM phase in the wire gradually shrunk, and after a temperature drop of 6 °C, the entire wire had transformed.

The Figure 4.8 compares interfaces for different wire widths. In the wider wires, the FM phase in the wire tends to merge with the FM phase at the edges of the pad, thus the phase interface is connected between the wire and the corner of the pad. This merging starts to break gradually for 800 nm and 600 nm wide wires. A wire with a width of only 300 nm shows a clear interface between the sides of the strip without any merging with the pad edges.

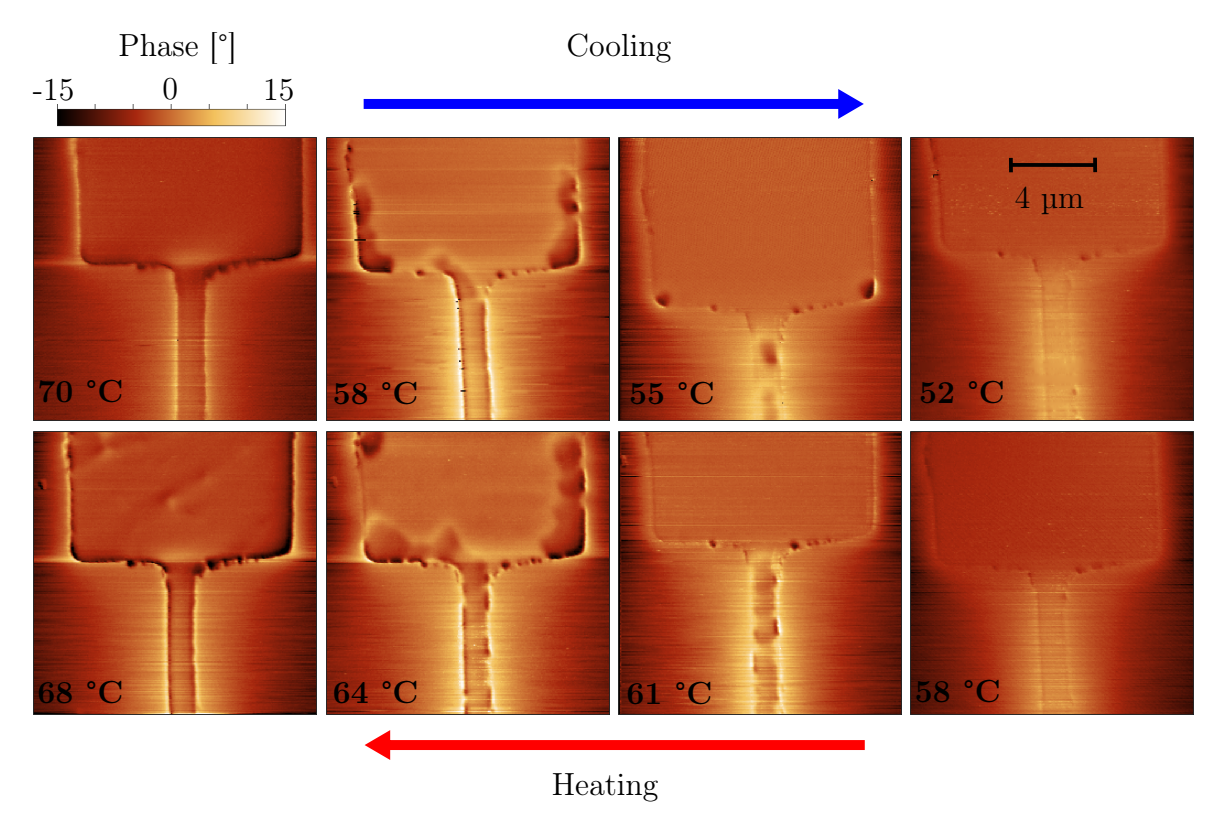


Figure 4.7: Comparison of cooling and heating of a 1000 nm wide, 25 µm thick wire with a 0° orientation. During cooling, there was a step change in the pad. Coexistence occurred and the desired phase interface between the strip and the continuous film was observed at 58 °C. During heating, the transformation of the films occurs with changing temperature similar to that during cooling. However, at 68 °C, small residues of AF phase are visible in the pad indicating that the pad transformation was gradual rather than stepwise during heating.

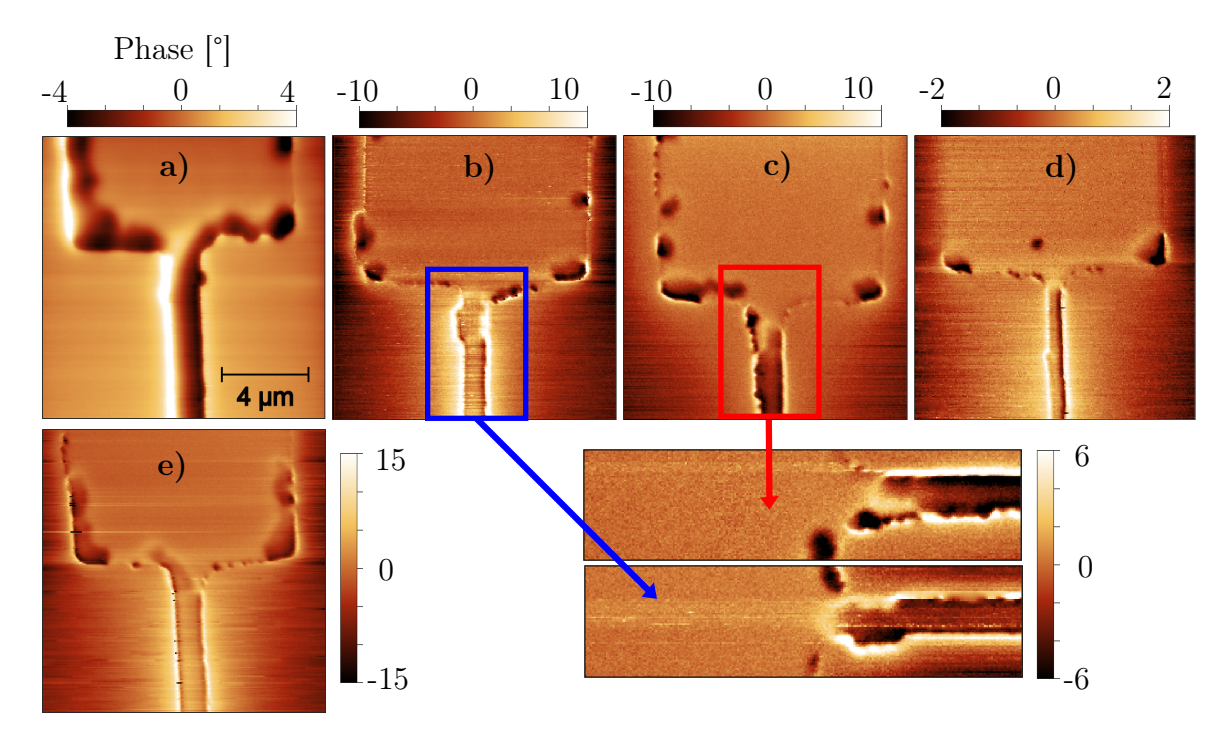


Figure 4.8: Comparison of the phase interface for wires of widths a) 1250 nm, b) 800 nm, c) 600 nm, d) 300 nm and e) 1000 nm at temperatures a) 63 °C, b) 54 °C, c) 54 °C, d) 58 °C nad e) 58 °C. As the interface for the 800 nm and 600 nm lengths is difficult to see due to the scanning direction, the detail of the wire was also measured with the scanning direction parallel to the wire to make the magnetic phase interface stand out.

Conclusions

In this bachelor thesis we have described the types of magnetic ordering, magnetic anisotropy and other important topics required in explanation of the magnetic behaviour of materials. We have described in detail the properties of FeRh and the phenomena associated with phase transformation.

Our experimental approach, supported by current literature research, involved depositing FeRh layers of 36 nm and 180 nm thicknesses, VSM characterization, subsequent patterning by electron beam lithography and characterization using Magnetic Force Microscopy. Our findings reveal a strong dependence of strain relaxation on the orientation of the nanostripe relative to the crystal structure of the substrate. Notably, we observe a more pronounced substrate effect at an orientation of 0° compared to 45°. Another important result is that the 36 nm thin FeRh layers do not exhibit a continuous phase boundary between the wire and the full film for 1000 nm or wider wires; but instead, they form small domains indicative of strain distribution within the structure and at the edges.

For layers of the 180 nm thickness, we observed a phase coexistence between the nanopatterned stripe and the 10 μ m \times 10 μ m pad for stripes longer than 25 μ m. We achieved well-defined interfaces for stripe widths ranging from 1250 nm to 300 nm. In structures with wider stripes, we note a merging of the ferromagnetic phase at the edges of the pad with the ferromagnetic phase in the nanostripe, leading to a curved interface. However, this merging gradually dissipates at the interface in the thinner stripes with dimensions of 800 nm and 600 nm. Remarkably, a stripe width of 300 nm exhibits a clear interface between the pad and the wire. During cooling, the pad showed an instantaneous transformation, after which the interface was observed in the temperature interval around 3 °C.

In the future, this well defined interface between the FM wire and AF film will be used for the study of posible coupling between the two phases using magnetoresistance. For the implementation of these measurements pads of significantly larger dimensions will be created so that they can be contacted by wirebonding. Obtaining the widest possible temperature range over which the interface exists would significantly simplify the execution of the experiment. Since the instantaneous transformation of the pad could indicate its supercooling, increasing the dimensions of the pad could also result in preventing its supercooling, which would lead to a widening of the temperature interval of interface existence.

Bibliography

- [1] S. Peng, D. Zhu, W. Li, and et al. Exchange bias switching in an antiferromagnet/ferromagnet bilayer driven by spin-orbit torque. *Nat Electron*, 3:757–764, 2020.
- [2] Weisheng Zhao. New generation of sot-mram based on exchange bias manipulation, Dec 2020.
- [3] Kebin Li, Yihong Wu, Zaibing Guo, Yuankai Zheng, Guchang Han, Jinjun Qiu, Ping Luo, Lihua An, and Tiejun Zhou. Exchange coupling and its applications in magnetic data storage. *Journal of Nanoscience and Nanotechnology*, 7(1):13–45, 2007.
- [4] Richard Phillips Feynman, Robert B. Leighton, and Matthew L. Sands. Feynmanovy přednášky z fyziky: revidované vydání s řešenými příklady. Fragment, Praha, 2. vydání edition, 2013.
- [5] Stephen Blundell. *Magnetism in Condensed Matter*. Oxford University Press Inc., New York, 1. vyd. edition, 2001.
- [6] X. Fan, T. G. Myers, B. A. D. Sukra, and G. Gabrielse. Measurement of the electron magnetic moment. *Phys. Rev. Lett.*, 130:071801, Feb 2023.
- [7] David Halliday, Robert Resnick, and Jearl Walker. *Fyzika*. VUTIUM, Brno, 2., přeprac. vyd. edition, 2013. Překlady vysokoškolských učebnic.
- [8] Prof. Barton Zwiebach. Lectures 20 and 21: Quantum Mechanics in 3D and Central Potentials. Physics MIT, Quantum Physics I, May 2016.
- [9] Marc Cahay Supriyo Bandyopadhyay. *Introduction to Spintronics*. CRC Press, 2. vyd. edition, 2020.
- [10] Olivier FRUCHART. Thanomagnetism. pages 2437–2445, September 2017.
- [11] Jonathan Keeling. Quantum Magnetism.
- [12] Puspamitra Panigrahi, C. Araujo, Tanveer Hussain, and Rajeev Ahuja. Crafting ferromagnetism in mn-doped mgo surfaces with p-type defects. Science and Technology of Advanced Materials, 15:035008, 06 2014.
- [13] D. Givord and Toshiro Takabatake. Magnetic Order. 12 2016.

- [14] Charles Kittel. Introduction to Solid State Physics. Wiley, 11 2004.
- [15] Xiaoyan Zhu, Yang Li, Yali Xie, Qian Qiu, Cuimei Cao, Xiao Hu, Wenhui Xie, Tian Shang, Yang Xu, Lin Sun, Wenjuan Cheng, Dongmei Jiang, and Qingfeng Zhan. Magnetocrystalline anisotropy of epitaxially grown ferh/mgo(001) films. Journal of Alloys and Compounds, 917:165566, 2022.
- [16] M T Johnson, P J H Bloemen, F J A den Broeder, and J J de Vries. Magnetic anisotropy in metallic multilayers. Reports on Progress in Physics, 59(11):1409, nov 1996.
- [17] L H Lewis, C H Marrows, and S Langridge. Coupled magnetic, structural, and electronic phase transitions in ferh. *Journal of Physics D: Applied Physics*, 49(32):323002, jul 2016.
- [18] L. J. Swartzendruber. The ferh (iron-rhodium) system. Bulletin of Alloy Phase Diagrams, 5(5):456–462, Oct 1984.
- [19] Jingfan Ye, Marco Hauke, Vikram Singh, Rajeev Rawat, Mukul Gupta, AKHIL TAYAL, S. M Amir, Jochen Stahn, and Amitesh Paul. Magnetic properties of ordered polycrystalline ferh thin films. RSC Advances, 7:44097, 09 2017.
- [20] G. Shirane, R. Nathans, and C. W. Chen. Magnetic moments and unpaired spin densities in the fe-rh alloys. *Phys. Rev.*, 134:A1547–A1553, Jun 1964.
- [21] E G Ponyatovskii, A R Kut-sar, and G T Dubovka. The possibility of the existence of a singular triple point on the pressure-temperature diagram of an iron-rhodium alloy. *Kristallografiya*, 12(1):79–83, 1967. Translated title: Soy. Phys. Crystallogr., 12(1), 63-66 (1967). (Pressure; Experimental).
- [22] Peter Eastman. Introduction to statistical mechanics.
- [23] Ecole Superieure Pierre Papon, Jacques Leblond. *The Physics of Phase Transition*. Editions Dunod, 1999.
- [24] P. Tu, A. J. Heeger, J. S. Kouvel, and J. B. Comly. Mechanism for the First-Order Magnetic Transition in the FeRh System. *Journal of Applied Physics*, 40(3):1368– 1369, 03 1969.
- [25] M Loving, F Jimenez-Villacorta, B Kaeswurm, D A Arena, C H Marrows, and L H Lewis. Structural evidence for stabilized ferromagnetism in epitaxial ferh nanoislands. *Journal of Physics D: Applied Physics*, 46(16):162002, apr 2013.
- [26] E. F. Bertaut, A. Delapalme, F. Forrat, G. Roult, F. De Bergevin, and R. Pauthenet. Magnetic Structure Work at the Nuclear Center of Grenoble. *Journal of Applied Physics*, 33(3):1123–1124, 03 1962.
- [27] G. Shirane, C. W. Chen, P. A. Flinn, and R. Nathans. Hyperfine Fields and Magnetic Moments in the Fe–Rh System. *Journal of Applied Physics*, 34(4):1044– 1045, 04 1963.

- [28] G. Shirane, R. Nathans, and C. W. Chen. Magnetic moments and unpaired spin densities in the fe-rh alloys. *Phys. Rev.*, 134:A1547–A1553, Jun 1964.
- [29] N I Medvedeva, D Van Aken, and J E Medvedeva. Magnetism in bcc and fcc fe with carbon and manganese. *Journal of Physics: Condensed Matter*, 22(31):316002, jul 2010.
- [30] J. S. Kouvel and C. C. Hartelius. Anomalous Magnetic Moments and Transformations in the Ordered Alloy FeRh. *Journal of Applied Physics*, 33(3):1343–1344, 03 1962.
- [31] J. M. Lommel. Magnetic and Electrical Properties of FeRh Thin Films. *Journal of Applied Physics*, 37(3):1483–1484, 03 1966.
- [32] Jon Ander Arregi, Friederike Ringe, Jan Hajduček, Olena Gomonay, Tomáš Molnár, Jiří Jaskowiec, and Vojtěch Uhlíř. Magnetic-field-controlled growth of magnetoelastic phase domains in ferh. *Journal of Physics: Materials*, 6(3):034003, may 2023.
- [33] Nao. Fujita, S. Kosugi, Y. Saitoh, Y. Kaneta, K. Kume, T. Batchuluun, N. Ishikawa, T. Matsui, and A. Iwase. Magnetic states controlled by energetic ion irradiation in FeRh thin films. *Journal of Applied Physics*, 107(9):09E302, 04 2010.
- [34] J. L. Warren, C. W. Barton, C. Bull, and T. Thomson. Topography dependence of the metamagnetic phase transition in ferh thin films. *Scientific Reports*, 10(1):4030, 2020.
- [35] S.A. Nikitin, G. Myalikgulyev, A.M. Tishin, M.P. Annaorazov, K.A. Asatryan, and A.L. Tyurin. The magnetocaloric effect in fe49rh51 compound. *Physics Letters A*, 148(6):363–366, 1990.
- [36] R. R. Gimaev, A. A. Vaulin, A. F. Gubkin, and V. I. Zverev. Peculiarities of magnetic and magnetocaloric properties of fe-rh alloys in the range of antiferromagnet-ferromagnet transition. *Physics of Metals and Metallography*, 121(9):823–850, 2020.
- [37] Radhika Barua, Félix Jiménez-Villacorta, and L. H. Lewis. Towards tailoring the magnetocaloric response in FeRh-based ternary compounds. *Journal of Applied Physics*, 115(17):17A903, 01 2014.
- [38] Pallavi Kushwaha, Archana Lakhani, R. Rawat, and P. Chaddah. Low-temperature study of field-induced antiferromagnetic-ferromagnetic transition in pd-doped fe-rh. *Phys. Rev. B*, 80:174413, Nov 2009.
- [39] Makoto Takahashi and Ryuichiro Oshima. Annealing effect on phase transition of equiatomic ferh alloy. *Materials Transactions*, *JIM*, 36(6):735–742, 1995.

- [40] Jon Ander Arregi, Ond řej Caha, and Vojt ěch Uhlíř. Evolution of strain across the magnetostructural phase transition in epitaxial ferh films on different substrates. *Phys. Rev. B*, 101:174413, May 2020.
- [41] Y. Ohtani and I. Hatakeyama. Features of broad magnetic transition in ferh thin film. *Journal of Magnetism and Magnetic Materials*, 131(3):339–344, 1994.
- [42] Andreas Herklotz, Dongkyu Lee, Er-Jia Guo, Tricia Meyer, Jonathan Petrie, and Ho Lee. Strain coupling of oxygen non-stoichiometry in perovskite thin films. Journal of Physics: Condensed Matter, 29:493001, 11 2017.
- [43] Min-Tae Park, Jiseok Yang, Junil Ahn, Sang il Seo, Woosuk Yoo, Young Haeng Lee, Hyobin Yoo, Kab-Jin Kim, and Myung-Hwa Jung. Impact of optimized growth conditions for magnetic phase transition and magnetic domain evolution in epitaxial ferh thin films. *Applied Surface Science*, 655:159539, 2024.
- [44] Ing. Jiří Jaskowiec. Vliv prostorového omezení na vlastnosti metamagnetických nanostruktur, 2019.
- [45] Jeongmin Hong, Tiannan Yang, Alpha T. N'Diaye, Jeffrey Bokor, and Long You. Effects of interface induced natural strains on magnetic properties of ferh. *Nano-materials*, 9(4), 2019.
- [46] C. W. Barton, T. A. Ostler, D. Huskisson, C. J. Kinane, S. J. Haigh, G. Hrkac, and T. Thomson. Substrate induced strain field in ferh epilayers grown on single crystal mgo (001) substrates. *Scientific Reports*, 7(1):44397, 2017.
- [47] Aleksei S. Komlev, Dmitriy Y. Karpenkov, Dmitry A. Kiselev, Tatiana S. Ilina, Alisa Chirkova, Radel R. Gimaev, Takamasa Usami, Tomoyasu Taniyama, Vladimir I. Zverev, and Nikolai S. Perov. Ferromagnetic phase nucleation and its growth evolution in ferh thin films. *Journal of Alloys and Compounds*, 874:159924, 2021.
- [48] C Baldasseroni, C Bordel, C Antonakos, A Scholl, K H Stone, J B Kortright, and F Hellman. Temperature-driven growth of antiferromagnetic domains in thin-film ferh. *Journal of Physics: Condensed Matter*, 27(25):256001, jun 2015.
- [49] V. Uhlíř, J. A. Arregi, and E. E. Fullerton. Colossal magnetic phase transition asymmetry in mesoscale ferh stripes. *Nature Communications*, 7(1):13113, 2016.
- [50] Lucie Motyčková. Epitaxial growth and characterization of metamagnetic nanoparticles for biomedical applications, 2018.
- [51] Mohsin Rafique. Study of the Magnetoelectric Properties of Multiferroic Thin Films and Composites for Device Applications. PhD thesis, 03 2015.
- [52] Wilhelm Melitz, Jian Shen, Andrew C. Kummel, and Sangyeob Lee. Kelvin probe force microscopy and its application. *Surface Science Reports*, 66(1):1–27, 2011.
- [53] Nanosurf. Afm working principle. Accessed on 2024-04-16.

 $[54]\,$ Molecular Vista. An introduction to a fm-ir, 2022.